

In the format provided by the authors and unedited.

Earthquake nucleation and fault slip complexity in the lower crust of central Alaska

Carl Tape^{ID 1*}, Stephen Holtkamp^{ID 1}, Vipul Silwal^{ID 1}, Jessica Hawthorne^{ID 2}, Yoshihiro Kaneko^{ID 3}, Jean Paul Ampuero^{ID 4,5}, Chen Ji^{ID 6}, Natalia Ruppert^{ID 1}, Kyle Smith^{ID 1} and Michael E. West^{ID 1}

¹Geophysical Institute, University of Alaska Fairbanks, Fairbanks, AK, USA. ²Department of Earth Sciences, University of Oxford, Oxford, UK. ³GNS Science, Lower Hutt, New Zealand. ⁴Seismological Laboratory, California Institute of Technology, Pasadena, CA, USA. ⁵Université Côte d'Azur, IRD, CNRS, Observatoire de la Côte d'Azur, Géoazur, France. ⁶Department of Earth Science, University of California, Santa Barbara, CA, USA. *e-mail: ctape@alaska.edu

Supplementary Information for Earthquake nucleation and fault slip complexity in the lower crust of central Alaska

Carl Tape, Stephen Holtkamp, Vipul Silwal, Jessica Hawthorne, Yoshihiro Kaneko,

Jean Paul Ampuero, Chen Ji, Natalia Ruppert, Kyle Smith, Michael E. West

correspondence to: ctape@alaska.edu

**Contains: Supplementary Figures 1–23,
Supplementary Tables 1–5, and Supplementary Text**

S1 The 2015 VLFE spectra as a sum of smaller events

It is possible to model the 2015 M_W 3.8 VLFE as the sum of about 10 M_W 3.2 earthquakes occurring over the course of about 10 seconds, following the approach *Gomberg et al.* (2016) used to model VLFEs as sums of much smaller LFEs.

To see this, imagine the VLFE is the sum of N subevents, all of which have moment M_{0s} and corner frequency f_{cs} , and source spectra

$$S_s(f) = M_{0s} \frac{1}{1 + (f/f_{cs})^2}. \quad (\text{S1})$$

At frequencies much lower than 0.05 Hz—far lower than 1 over the VLFE duration—all of the subevents will occur during a small portion of the period of interest and combine constructively, giving low-frequency VLFE spectral amplitude proportion to the VLFE moment

$$S_v(f \ll 0.05 \text{ Hz}) = NS_s(f) = NM_{0s}. \quad (\text{S2})$$

At frequencies much higher than 0.05 Hz—far higher than 1 over the VLFE duration—the subevents will occur during random portions of the period of interest and may combine constructively or destructively. In this case, the VLFE amplitude will be given by

$$S_s(f \gg 0.05 \text{ Hz}) = \sqrt{N} S_s(f) = \sqrt{N} M_{0s} \frac{1}{1 + (f/f_{cs})^2}. \quad (\text{S3})$$

These are the two end member regimes in the approach of *Gomberg et al.* (2016). At intermediate frequencies, the VLFE amplitude $S_v(f)$ will be between $\sqrt{N} S_s(f)$ and $NS_s(f)$.

These VLFE source spectra may be observed via displacement spectra at the station. The

displacement spectra at a given frequency are given by the source spectra $S_v(f)$ multiplied by a path effect $G(f)$. So to analyze the 2015 VLFE, it is useful to compare its spectra with the spectra of a nearby M_W 3.5 earthquake. We model the spectra of the M_W 3.5 earthquake with moment M_{0e} and corner frequency f_{ce} as

$$S_e(f) = M_{0e} \frac{1}{1 + (f/f_{ce})^2}. \quad (\text{S4})$$

At frequencies larger than 1 Hz, the 2015 VLFE and M_W 3.5 earthquake have similar displacement spectra, as seen in Figure S6d.

Equating the high-frequency VLFE spectrum to the M_W 3.5 spectrum and assuming they have the same path effect gives

$$S_s(f \gg 0.05 \text{ Hz})G(f) = S_e(f)G(f) \quad (\text{S5})$$

$$\sqrt{N}M_{0s} \frac{1}{1 + (f/f_{cs})^2} = M_{0e} \frac{1}{1 + (f/f_{ce})^2}. \quad (\text{S6})$$

Since the two spectra have similar shapes at high frequency, we may assume that they have similar corner frequencies f_{cs} and f_{ce} , and estimate that

$$\sqrt{N}M_{0s} = M_{0e}, \quad (\text{S7})$$

where M_{0e} is the moment of a M_W 3.5 earthquake. However, we also have inferred from the analysis of the low-frequency VLFE signal (or from the $\ll 0.05$ Hz VLFE amplitude, if you prefer) that the VLFE moment M_{0v} is equivalent to a M_W 3.8 earthquake. Matching the VLFE moment with N subevents with moment M_{0s} gives

$$NM_{0s} = M_{0v} = \text{moment of } M_w 3.8 \text{ earthquake.} \quad (\text{S8})$$

Combining the high-frequency and moment constraints (equations (S7) and (S8)) gives

$$\sqrt{N} \frac{M_{0v}}{N} = M_{0e} \quad (\text{S9})$$

$$\sqrt{N} = \frac{M_{0v}}{M_{0e}} \quad (\text{S10})$$

$$N = \left(\frac{\text{moment of } M_w 3.8 \text{ earthquake}}{\text{moment of } M_w 3.5 \text{ earthquake}} \right)^2 \approx 8. \quad (\text{S11})$$

So it is possible to match the data by constructing the M_W 3.8 VLFE from 8 M_W 3.2 earthquakes.

These 8 subevents are consistent with the 10 or so peaks observed in the deconvolution of the 2015 VLFE (Figure S4a).

To match the spectral shape, those M_W 3.2 earthquakes would have to have corner frequencies similar to the M_W 3.5 earthquake analyzed for comparison. Commonly observed corner frequency scaling suggests that M_W 3.2 earthquakes should have corner frequencies a factor of

1.4 higher than M_W 3.5 earthquakes, so the lower subevent corner frequencies might suggest slightly lower stress drop or rupture velocities for the VLFE subevents, but that level of variation in the corner frequency, coupled with variability in the spectra, is within the range observed in earthquakes, so it is plausible that the VLFE subevents could be normal earthquakes.

We note, however, that it is very rare to observe 8 M_W 3.2 earthquakes within a 10-second interval without a strong external forcing. So any physical model of VLFEs as a sum of subevents would likely require a driving mechanism distinct from that commonly seen in normal earthquakes, be it fluid diffusion, off-fault microcracking, delayed nucleation, or aseismic slip.

Indeed, we should note that our preferred slow slip interpretation and the VLFE as a sum of subevents are end members, and one could model part of the VLFE moment via subevents and part of the moment as aseismic slip. In that case, the total VLFE moment M_{0v} modeled as subevents in equation (S11) would be smaller, and a larger number of smaller subevents would be expected. However, if such smaller subevents exist, they would be expected to have higher corner frequencies, and the VLFE spectra would also be expected to have more power at higher frequencies—to have a slower high-frequency decay than the M_W 3.5 earthquake used for comparison. Such a model would appear to contradict the observations. However, the contradiction could arise because the model is overly simplistic. It may not be appropriate to assume that there are 100 or more earthquakes of a similar size. If there are many events of different sizes, the high-frequency spectra could have a different shape, determined by the subevent size distribution rather than their average corner frequency.

S2 The low-frequency foreshock signal of the 2016 event

S2.1 Low-frequency onset of the 2016 event

Figures S10–S12 show low-frequency causal filtered seismograms and high-frequency envelopes for all 17 stations within 60 km of the 2016 earthquake. The origin time of the 2016 earthquake (dashed line corresponding to the origin of the x -axis) is shown along with P and S phase picks on the envelope plot. On the low-frequency plots, we pick the onset of the low-frequency waves associated with the event. Low-frequency picks preceding the P-wave arrival of the mainshock—interpreted as the precursory VLFE—are present on 8 of the 17 closest stations (Table S3, Figures S10–S12).

S2.2 Relative timing of foreshock signals for the 2016 event

The onset times of HFF and LFF for the 2016 event are listed in Table S4. The column LF-HF shows the difference between the onsets, while the last column (LF-HF-10) shows the difference between the onsets, but with a 10-second correction applied to LF on the basis of Figure S9. Here we consider the three possibilities for the relative timing of the HFF and LFF signals for the 2016 event.

- **Option 1 (preferred): HFF and LFF are simultaneous.** The last column in Table S4, which has the 10-second correction (Figure S9), shows values that are near 0 s, indicating that the HFF and LFF are nearly simultaneous.
- **Option 2: LFF before HFF.** It is possible that the LFF signals occurred before HFF. Three factors could promote an earlier initiation of LFF:
 1. The delay in the measured onset time is greater than the 8–12 s implied by Figure S9. This would push the actual LFF onset time earlier.
 2. A portion of LFF is below our detection capabilities. This would imply that the actual LFF started earlier than it was detected. The LFF has a simple long-period pulse (Figure 2b), but it is barely detectable on even the closest stations, whereas HFF is easily detected on all stations (Table S3).
 3. The delay could be a consequence of differences in seismic velocities. Although we have rotated the seismograms to analyze the transverse component, the earliest arriving HFF signal is likely P waves, while the LFF signal is comprised of shear or surface waves. Given the depth of the event and monitoring network, this could introduce a delay of the LFF arrivals of a few to several seconds.
- **Option 3: HFF before LFF.** If the delay in the measured onset time of LFF is less than the 8–12 s implied by Figure S9, then HFF would appear to start before LFF is observed.

For the 2015 event, option 3 is clearly the case: we see that $LF-HF-10 > 20$ for most stations within 50 km of the event (Table S5), indicating a clear delay of LF with respect to HF. We also see that the low-frequency signal started near or just after the peak in the high-frequency waves, evidenced from the positive values of LF in Table S5.

Our observations can be reconciled with our interpretations in Figure 4 and Table S2, which propose that aseismic slow slip was responsible for the growing high-frequency signals of the 2015 and 2016 events. For the 2016 event, the duration of the aseismic slip could have been absent, since the LFF—representing a VLFE—and HFF are nearly coincident. For the 2015 event, the duration of aseismic slip is inferred to be ~ 20 s (Table S5) before transitioning into a VLFE (e.g., Figure S1).

Supplementary Table S1: Events in Minto Flats fault zone in this study and in *Tape et al.* (2015). The subregion corresponds to the designation in *Tape et al.* (2015). The depth is from the moment tensor inversion, with the catalog depth in parentheses. The duration listed is the one used within the moment tensor inversion, if performed. The bandpass for each moment tensor inversion is listed as the periods T_1 and T_2 . VLFE = very-low-frequency earthquake, HFS = increasing high-frequency signal, EQ = earthquake. Y-I denotes that we interpret the event as a VLFE based on the HFS.

origin time	subregion	latitude	longitude	M_w	M_l	depth (km)	duration (s)	T_1 (s)	T_2 (s)	VLFE	HFS	EQ
events in <i>Tape et al.</i> (2015):												
2000-11-29 10:35:47.2	S	63.90	-150.35	5.7	5.8	19 (16.4)	7.1	20	40	-	-	Y
2000-12-06 18:40:26.0	S	63.89	-150.31	4.9	5.0	10 (11.7)	2.8	20	33.3	-	-	Y
2001-03-25 11:34:50.9	E	64.63	-149.25	4.4	4.6	20 (22.2)	1.6	16.7	40	-	-	Y
2001-06-30 09:41:42.3	S	64.04	-150.15	4.6	4.4	16 (14.6)	2.0	14.3	25	-	-	Y
2008-07-16 10:12:00.6	W	64.59	-149.53	3.9	4.1	23 (30.5)	1.0	16.7	25	-	-	Y
2009-07-28 12:13:15.7	W	64.61	-149.49	3.8	3.7	23 (22.7)	1.0	14.9	25	-	-	Y
2012-04-11 09:21:57.4	W	64.92	-148.95	3.8	3.9	16 (19.3)	1.0	1.7	3.3	Y-I	Y	Y
2013-03-05 21:55:58.4	E	64.84	-148.73	3.4	3.4	20 (17.3)	1.0	16.7	28.6	-	-	Y
2013-06-05 18:58:23.3	SW	64.64	-149.68	3.9	4.0	10 (13.9)	1.0	16.7	33.3	-	-	Y
2013-07-12 07:59:17.0	N	65.09	-148.77	3.6	3.4	16 (17.2)	1.0	10	22.2	-	-	Y
2014-12-13 15:47:31.4	E	64.43	-149.38	3.4	3.3	17 (13.0)	1.0	11.1	28.6	-	-	Y
events in this study:												
2002-12-29 20:38:30.2	E	64.95	-148.61	-	3.4	- (17.6)	-	-	-	-	-	Y
2004-11-17 11:29:00.3	W	64.89	-149.10	-	3.6	- (18.8)	-	-	-	-	-	Y
2011-11-18 10:46:23.5	W	64.94	-148.94	-	3.4	- (11.1)	-	-	-	-	-	Y
2013-03-12 07:39:50.2	E	64.72	-148.95	3.5	2.1	23 (1.0)	12	25	40	Y	Y	-
2015-09-12 03:24:12.2	N	65.13	-148.67	-	1.4	- (20.4)	-	-	-	Y-I	Y	-
2015-09-12 03:25:12.7	N	65.12	-148.66	3.8	2.6	21 (15.6)	10	20	50	Y	Y	-
2015-10-22 13:16:15.8	E	64.73	-149.04	2.6	2.7	18 (18.8)	1.0	5	20	-	-	Y
2015-10-31 02:56:35.6	S	64.43	-149.70	3.4	3.5	25 (23.9)	1.0	10	25	-	?	Y
2016-01-14 19:04:10.7	W	64.68	-149.25	3.7	3.8	17 (22.7)	1.0	10	30	Y	Y	Y

Supplementary Table S2: Summary of seismic observations for six events in this study from high-frequency waveforms (≥ 1 Hz;) and low-frequency waveforms (≤ 0.1 Hz;). Event locations are shown in Figure 1.

observation	stage in Fig. 4	2012 VLFE	2012 EQ	2013 VLFE	2015 VLFE	2015- 10-22 EQ	2015- 10-31 EQ	2016 VLFE	2016 EQ
growing high-frequency signal (Fig. 1b)	1								
simultaneous large-amplitude low-frequency signal	1								
earthquake (P, S, surface waves)	2								
AEC [†] catalog magnitude (M_l), from high frequencies			3.9	2.1	2.6	2.7	3.5		3.8
moment tensor magnitude (M_w), from low frequencies			3.8	3.5	3.8	2.6	3.4		3.7

[†]Alaska Earthquake Center

Supplementary Table S3: Polarities of waves (U = up, D = down) for the 2016-01-14 earthquake for stations within 200 km of the epicenter. LFFP = low-frequency foreshock polarity; HFP = high-frequency P polarity from earthquake; LFP = polarity predicted from low-frequency waveforms; parentheses denote stations that are nodal for the source mechanism (Fig. S3b). The LFFP picks are based on waveforms shown in Figures S10–S12, which show the vertical component of velocity, bandpass filtered 20–100 s. The amplitude listed is the amplitude at the peak of the LFFP.

stations		distance (km)	azimuth (°)	LFFP (nm/s)	HFP	LFP
F1TN	XV	5.3	127	–	–	(D)
F2TN	XV	6.2	62	–	U	U
FPAP	XV	10.5	138	D (-13.7)	D	D
F3TN	XV	11.0	26	–	U	(U)
FNN1	XV	12.5	173	D (-38.2)	D	D
NEA2	AK	13.2	140	D (-20.0)	D	D
FNN2	XV	15.2	218	U? (11.8)	D	(U)
FAPT	XV	16.8	152	D (-25.2)	D	D
F4TN	XV	17.4	15	D (-21.4)	–	(D)
FTGH	XV	20.1	87	U (24.7)	U	U
F5MN	XV	22.9	8	D (-26.0)	D	D
F6TP	XV	25.6	325	D (-32.1)	D	D
F7TV	XV	33.5	305	–	D	(D)
F8KN	XV	33.8	286	–	U	U
I23K	TA	52.1	354	–	D	D
BWN	AK	56.9	182	–	D	D
MDM	AK	57.3	57	–	U	U
WRH	AK	60.2	112	–	–	U
CCB	AK	69.0	93	–	U	U
COLA	IU	69.3	72	–	–	U
POKR	TA	98.6	60	–	–	U
BPAW	AK	106.1	233	–	–	U
MCK	AK	107.1	172	–	–	D
HDA	AK	114.5	104	–	–	U
PS08	PS	117.1	97	–	–	U
I21K	TA	140.7	294	–	–	U
RND	AK	143.6	172	–	–	D
H24K	TA	143.7	26	–	–	D
TRF	AK	146.5	201	–	–	(D)
KTH	AK	150.1	214	–	–	U
CHUM	AK	173.3	240	–	–	U
CAST	AK	197.6	226	–	–	U
PPD	AK	198.2	60	–	–	D
H21K	TA	199.0	305	–	–	U

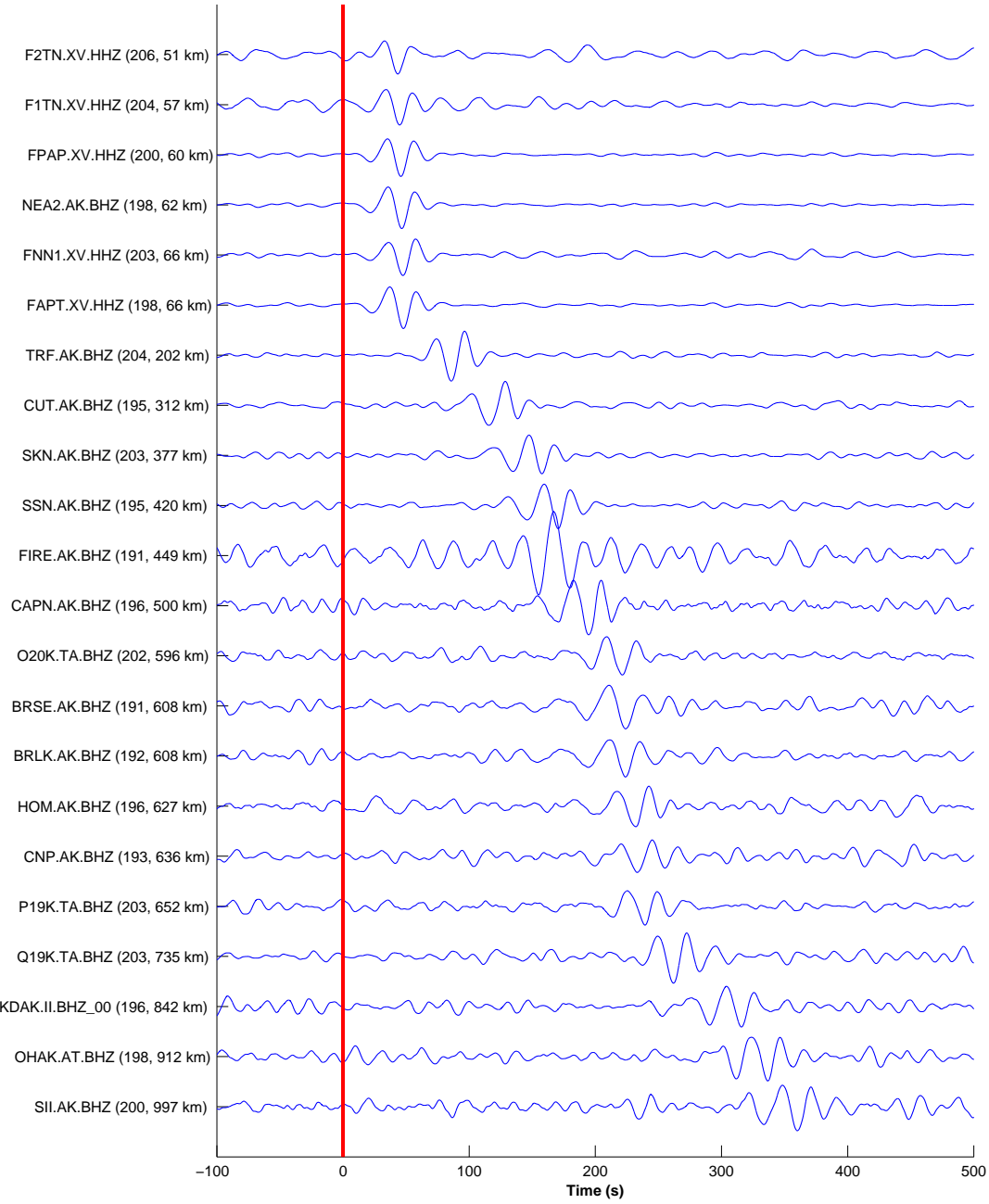
Supplementary Table S4: Time picks for the 2016 event. HF = HFF start time (emerges from background noise level). LF = LFF start time, only listed for the unequivocal polarity measurements in Table S3. HF and LF are relative to the P time of the M_w 3.7 earthquake. The differential time LF–HF is the delay in the LF onset relative to the HF onset. The time LF–HF–10 includes a 10-second correction in LF that is based on Figure S9.

stations		distance (km)	azimuth (°)	HF (s)	LF (s)	LF-HF (s)	LF-HF-10 (s)
F1TN	XV	5.3	127	-19.3	NaN	NaN	NaN
F2TN	XV	6.2	62	-18.8	NaN	NaN	NaN
FPAP	XV	10.5	138	-19.3	-9.5	9.8	-0.2
F3TN	XV	11.0	26	-18.3	NaN	NaN	NaN
FNN1	XV	12.5	173	-19.5	-11.0	8.5	-1.5
NEA2	AK	13.2	140	-20.6	-10.3	10.4	0.4
FNN2	XV	15.2	218	-21.7	NaN	NaN	NaN
FAPT	XV	16.8	152	-16.5	-11.1	5.3	-4.7
F4TN	XV	17.4	15	-18.9	-1.3	17.7	7.7
FTGH	XV	20.1	87	-20.9	-11.6	9.4	-0.6
F5MN	XV	22.9	8	-21.2	-12.1	9.1	-0.9
F6TP	XV	25.6	325	-20.3	-10.8	9.5	-0.5
F7TV	XV	33.5	305	-18.4	NaN	NaN	NaN
F8KN	XV	33.8	286	-20.9	NaN	NaN	NaN
I23K	TA	52.1	354	-19.6	NaN	NaN	NaN
BWN	AK	56.9	182	-21.0	NaN	NaN	NaN
MDM	AK	57.3	57	-19.6	NaN	NaN	NaN
WRH	AK	60.2	112	-21.4	NaN	NaN	NaN
CCB	AK	69.0	93	-19.6	NaN	NaN	NaN
COLA	IU	69.3	72	-19.7	NaN	NaN	NaN
POKR	TA	98.6	60	-18.4	NaN	NaN	NaN
BPAW	AK	106.1	233	-19.7	NaN	NaN	NaN
MCK	AK	107.1	172	-19.0	NaN	NaN	NaN
HDA	AK	114.5	104	-18.8	NaN	NaN	NaN
PS08	PS	117.1	97	-18.5	NaN	NaN	NaN
I21K	TA	140.7	294	-19.2	NaN	NaN	NaN
RND	AK	143.6	172	-17.7	NaN	NaN	NaN
H24K	TA	143.7	26	-18.1	NaN	NaN	NaN
TRF	AK	146.5	201	-19.8	NaN	NaN	NaN
KTH	AK	150.1	214	-19.0	NaN	NaN	NaN
CHUM	AK	173.3	240	-14.9	NaN	NaN	NaN
CAST	AK	197.6	226	-19.3	NaN	NaN	NaN
PPD	AK	198.2	60	-15.0	NaN	NaN	NaN
H21K	TA	199.0	305	-14.3	NaN	NaN	NaN

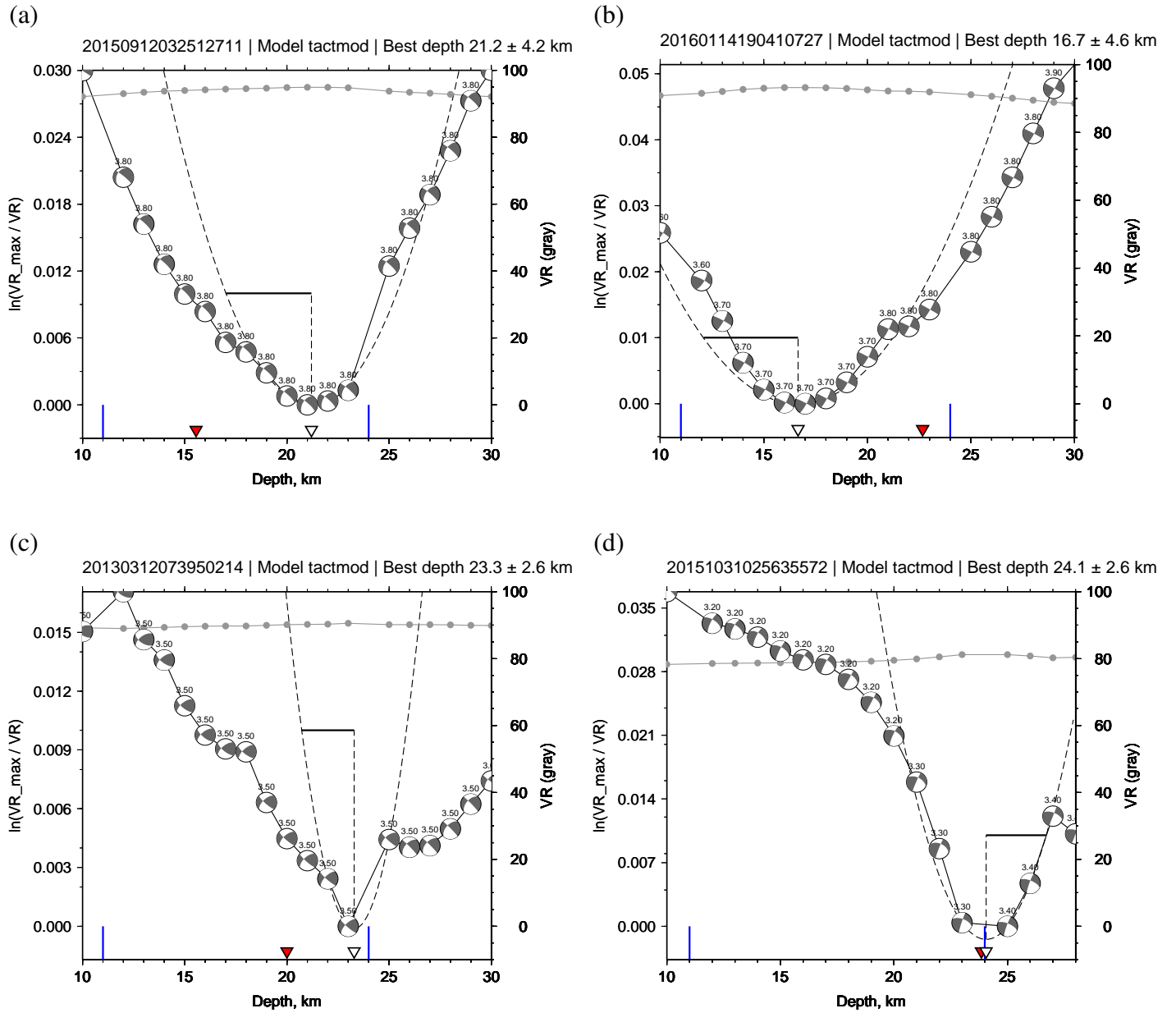
Supplementary Table S5: Time picks for the 2015 event. HF = HF start time. LF = LF start time. Both times are listed relative to the peak HF signal, which is estimated using a triangle fit to the 2–8 Hz filtered seismogram (e.g., Figure 1b). The differential time LF-HF is the delay in the LF onset relative to the HF onset. The time LF-HF-10 includes a 10-second correction in LF that is based on Figure S9.

stations		distance (km)	azimuth (°)	HF (s)	LF (s)	LF-HF (s)	LF-HF-10 (s)
MDM	AK	27.1	131	-20.9	8.5	29.4	19.4
PS07	PS	27.8	40	-21.8	NaN	NaN	NaN
I23K	TA	32.8	276	-23.2	-10.1	13.1	3.1
F5MN	XV	35.8	223	-27.3	2.9	30.1	20.1
F4TN	XV	39.4	216	-29.7	4.8	34.5	24.5
F3TN	XV	45.1	211	-31.7	5.0	36.7	26.7
TCOL	TA	46.8	126	-25.7	4.0	29.6	19.6
COLA	IU	46.8	126	-24.8	5.8	30.6	20.6
FTGH	XV	48.5	189	-25.4	5.5	31.0	21.0
F6TP	XV	50.6	237	-28.1	3.4	31.5	21.5
F2TN	XV	51.0	206	-27.4	11.2	38.6	28.6
F1TN	XV	57.0	204	-29.5	9.9	39.4	29.4
POKR	TA	57.8	90	-26.2	-7.0	19.2	9.2
FPAP	XV	60.2	200	-29.7	2.0	31.8	21.8
NEA2	AK	61.9	198	-28.0	4.9	32.9	22.9
F7TV	XV	62.4	242	-28.6	9.4	38.0	28.0
FNN1	XV	66.6	204	-34.3	5.5	39.8	29.8
FAPT	XV	66.7	198	-31.8	0.9	32.7	22.7
CCB	AK	66.8	142	-26.5	12.6	39.1	29.1
FNN2	XV	71.2	212	-30.8	2.5	33.3	23.3
F8KN	XV	71.8	237	-27.3	4.9	32.2	22.2
WRH	AK	77.3	159	-28.7	3.9	32.6	22.6
H24K	TA	87.8	24	-30.4	6.1	36.5	26.5
H23K	TA	88.5	333	-30.7	-5.2	25.5	15.5
PS06	PS	95.7	329	-30.9	NaN	NaN	NaN
MLY	AK	98.3	265	-31.5	-4.0	27.5	17.5
PS08	PS	108.7	126	-31.9	NaN	NaN	NaN
BWN	AK	109.9	196	-34.5	-9.7	24.7	14.7
HDA	AK	113.9	133	-32.7	1.7	34.4	24.4
PPD	AK	152.9	72	-32.5	21.7	54.1	44.1
MCK	AK	155.4	185	-39.7	7.6	47.3	37.3
I21K	TA	155.8	274	-42.0	-1.8	40.2	30.2
BPAW	AK	159.1	225	-40.2	-0.6	39.6	29.6
J25K	TA	166.1	108	-40.4	-4.3	36.0	26.0
RND	AK	191.4	183	-45.1	9.5	54.6	44.6

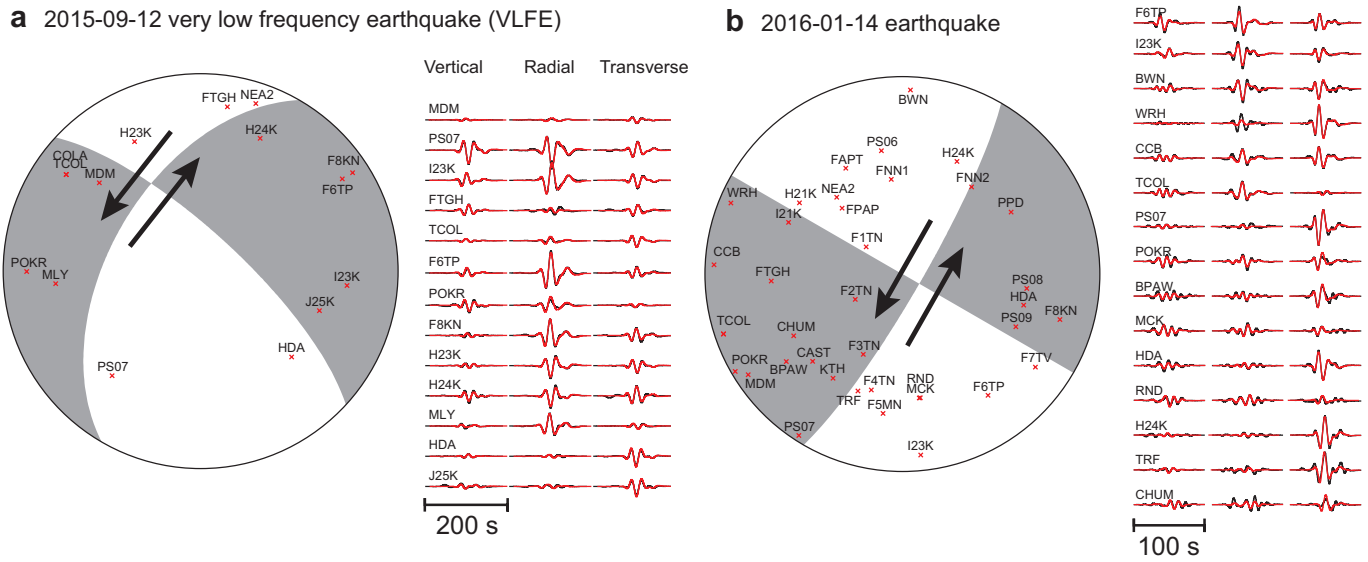
2015–09–12 03:23:32 + 600.00 s; F2TN max $-8.72e-01$ nm / sec at $t = 43.5$ s
 BHZ BHZ_00 HHZ [nm / sec, —] event 20150912032512711 (2015–09–12, M2.6, -148.7 , 65.1 , $z = 15.6$ km)
 22 / 22 seismograms (22 stations) ordered by input, norm $\rightarrow (\sin D)^{-0.50}$



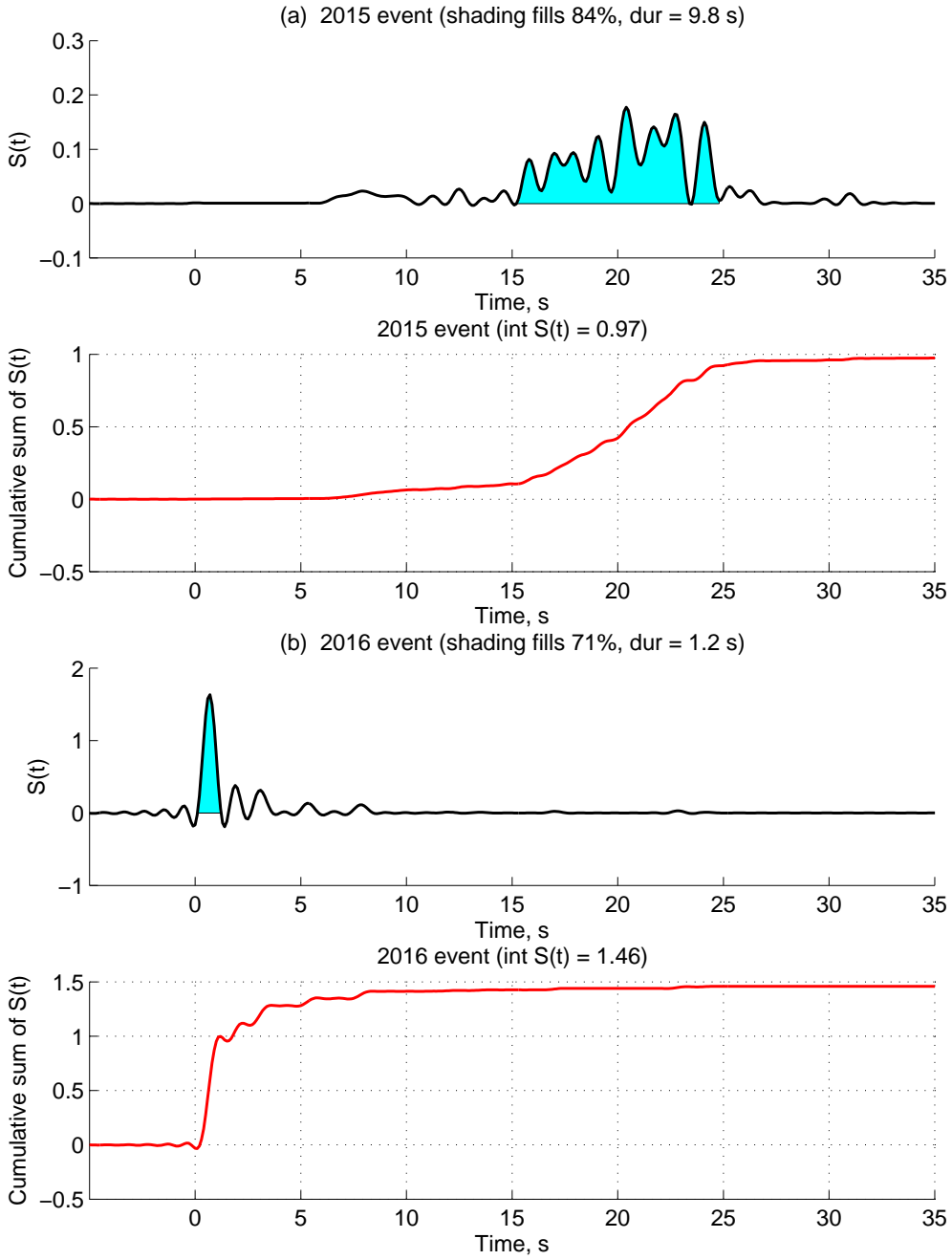
Supplementary Figure S1: Record section of vertical component velocity seismograms, filtered 20–50 s, for the M_w 3.8 2015 VLFE. Amplitudes have been corrected for geometric spreading of surface waves. The record section shows all stations within an azimuthal sector (here, 190° to 210°), such that the waveforms would be expected to be similar, since the source-station paths are similar. By cross-correlating all waveforms for this earthquake, we estimate a group velocity of 3.5 km/s.



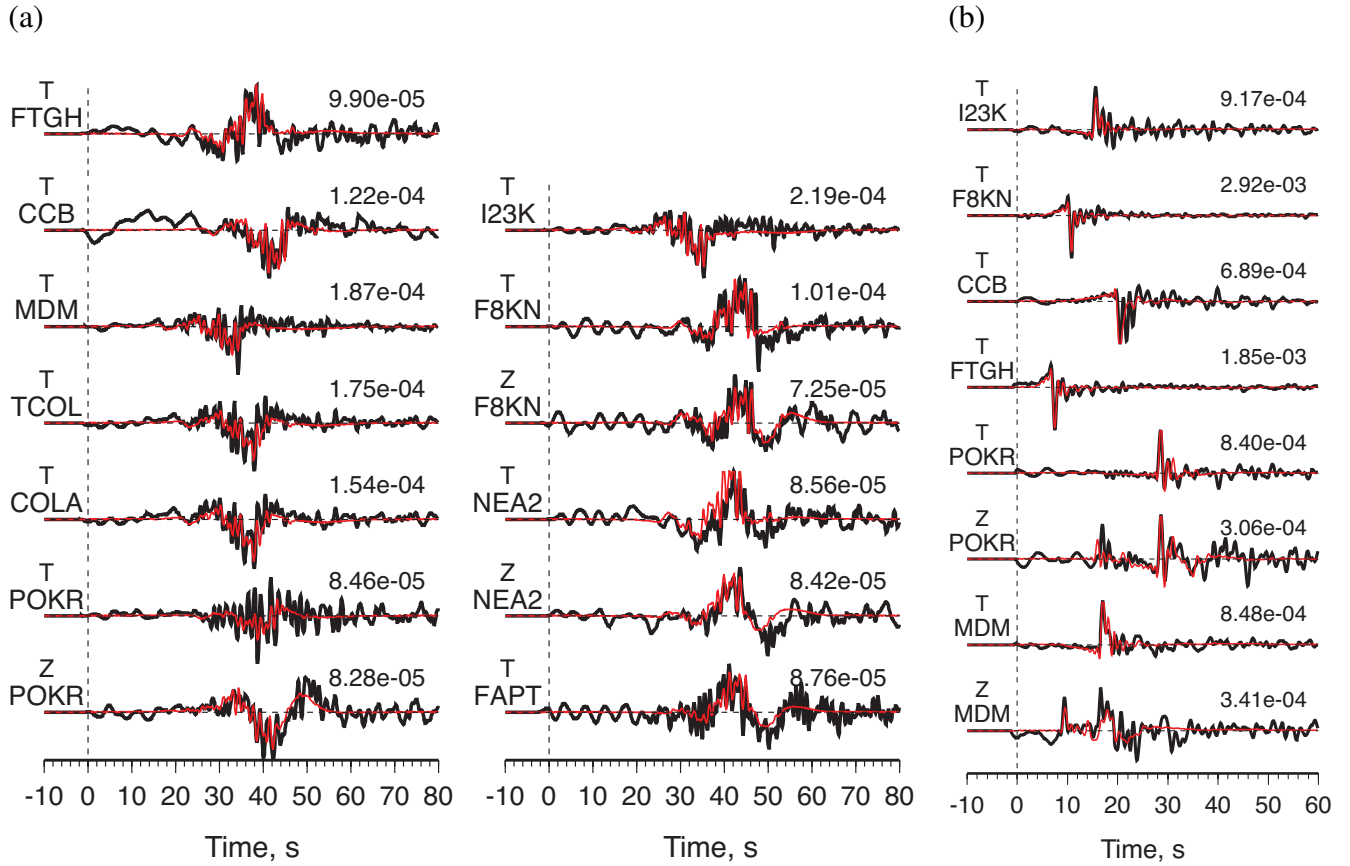
Supplementary Figure S2: Grid search over depth for four events in this study. For each depth, the moment tensor inversion allows the magnitude and orientation to vary. The red arrow is the AEC catalog depth derived from arrival times. The white arrow is the depth derived from the moment tensor inversion. (a) Grid search over depth for the 2015 event; the best-fitting depth is 21 ± 4 km. (b) Grid search over depth for the 2016 event; the best-fitting depth is 17 ± 5 km. (c) Grid search over depth for the 2013 event; the best-fitting depth is 23 ± 3 km. (d) Grid search over depth for the 2015-10-31 $M_w 3.4$ earthquake; the best-fitting depth is 18 ± 3 km. This earthquake is used for comparison in Figure S6. See Silwal (2018) for full results.



Supplementary Figure S3: Source mechanisms and waveform fits for the 2015 very-low-frequency earthquake (VLFE) (a) and the 2016 VLFE+earthquake (b). The beachball is a lower-hemisphere projection of the P-wave radiation pattern. The subset of waveform fits show the observations (black) in comparison with the modeled seismograms (red). See *Silwal (2018)* for full results.

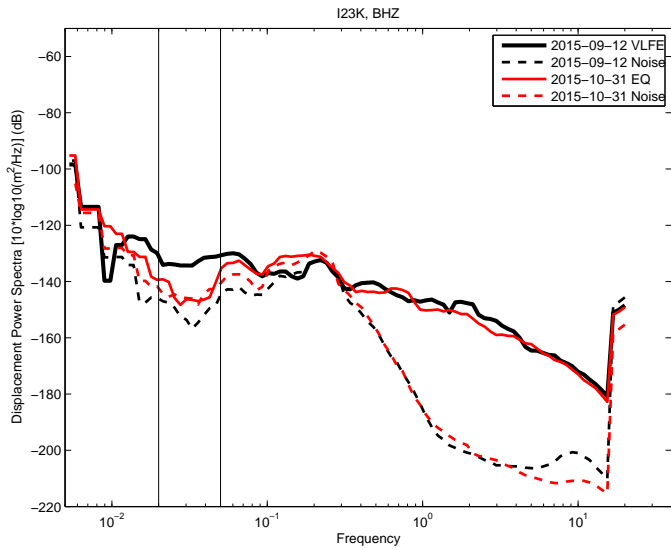


Supplementary Figure S4: Estimated source time functions for the 2015 and 2016 events, using seismograms filtered with $f \geq 1$ Hz. Each pair of plots shows the estimated source time function (top)—including a shaded portion that represents our interpretation of the source duration—as well as a cumulative (integrated) version of the source time function (bottom). (a) Source time function $S(t)$ for the 2015 very-low-frequency earthquake. The estimated duration of ~ 10 s is represented by the shaded maximum pulse, which fills 84% of the integrated area of $S(t)$. The magnitude of M_w 3.8 estimated from long-period waveforms (Figure S3b) matches the estimated moment from high-frequency waveforms. (b) Source time function $S(t)$ for the 2016 earthquake, estimated using the stations shown in Figure S5. The estimated duration of ~ 1 s is represented by the shaded maximum pulse. The magnitude of M_w 3.7 estimated from long-period waveforms (Figure S3a) matches the estimated moment from high-frequency waveforms after the main pulse, indicated by $\int S(t) \approx 1$ (red curve). We attribute the later, lower-amplitude pulses in $S(t)$ to noise. See Figure S13 for a source time function estimated using higher frequency waveforms.

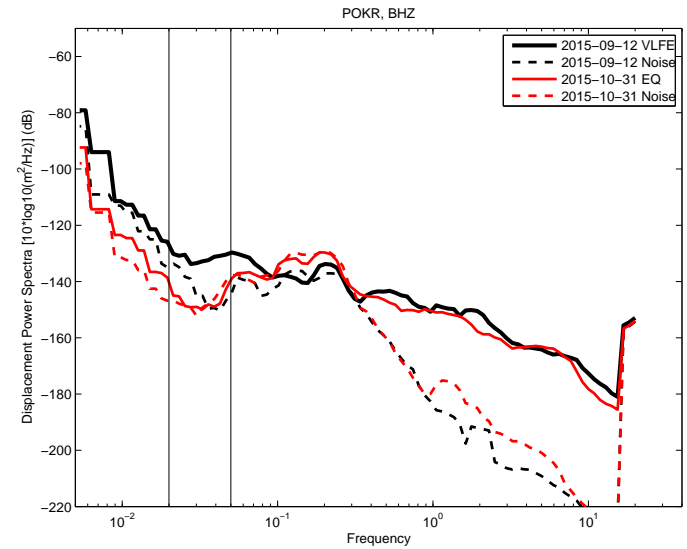


Supplementary Figure S5: Corresponding fits between synthetic seismograms (red) and observed seismograms for the source-time functions shown in Figure S4. In order to obtain better agreement between data and synthetics, they are bandpass filtered 1–50 s; excluding the shorter periods leads to a source duration estimate that is slightly longer (by ~ 0.5 s) than actuality. The max amplitudes in the data are listed in cm/s for each seismogram. All stations are < 100 km from the epicenter (Tables S4 and S5). (a) The 2015 M_w 3.7 very-low-frequency earthquake. (b) The 2016 M_w 3.7 earthquake.

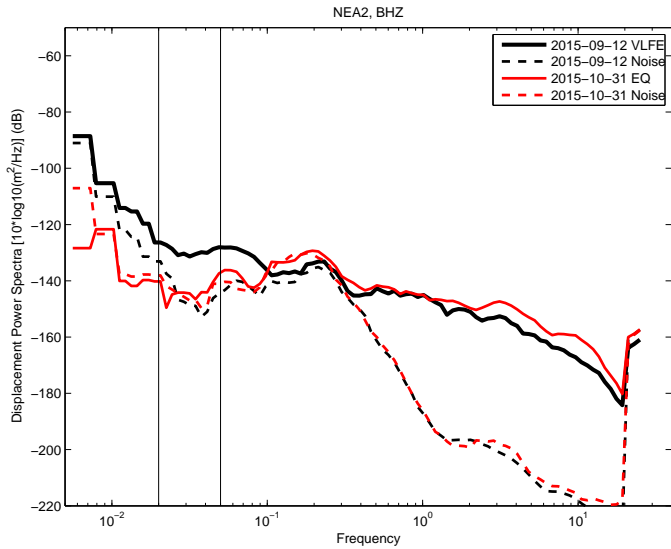
(a) TA.I23K (32.8 km, 81.8 km)



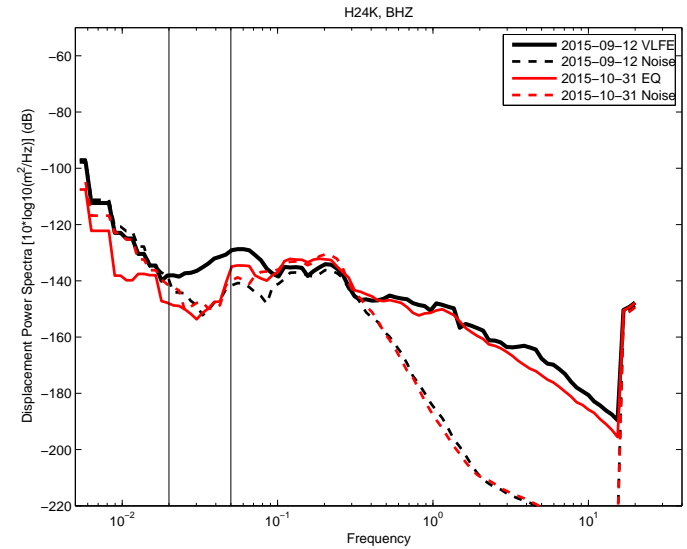
(b) TA.POKR (57.8 km, 132.2 km)



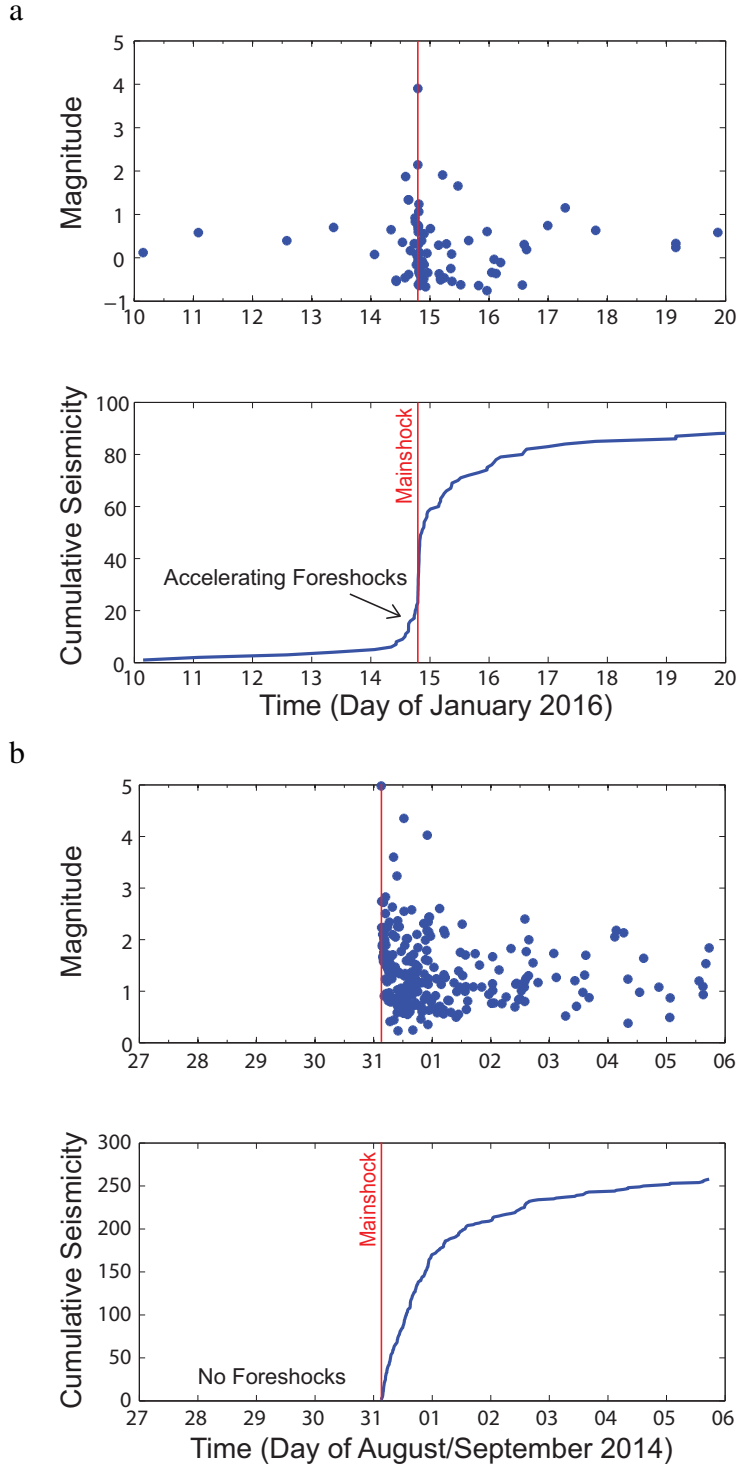
(c) AK.NEA2 (61.9 km, 35.3 km)



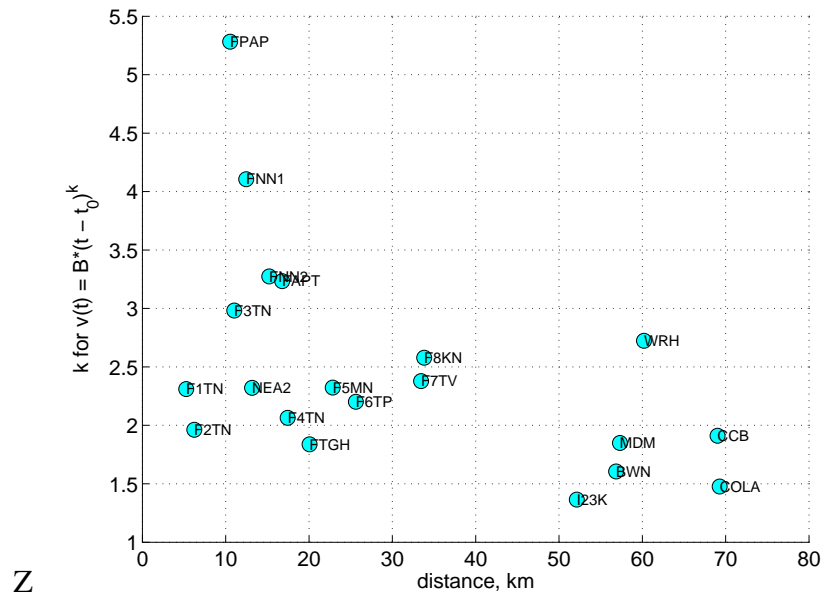
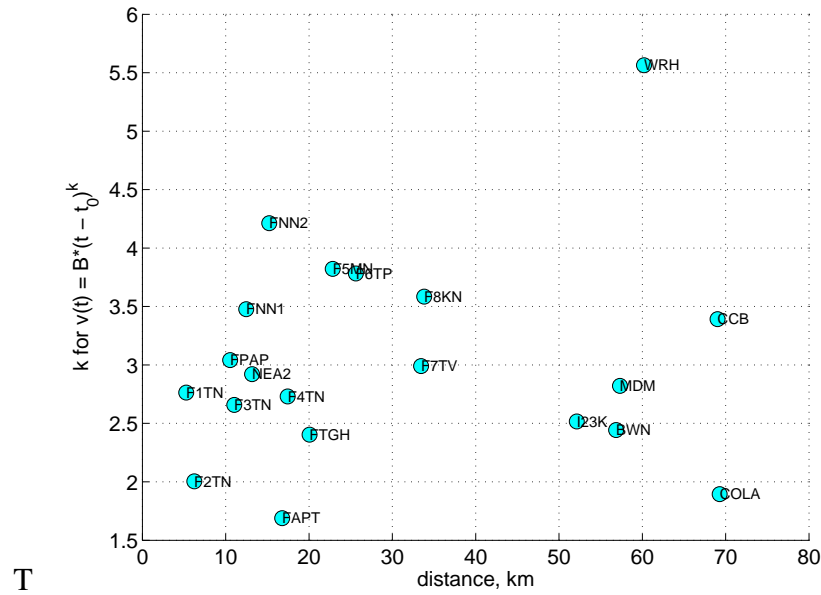
(d) TA.H24K (87.8 km, 178.7 km)



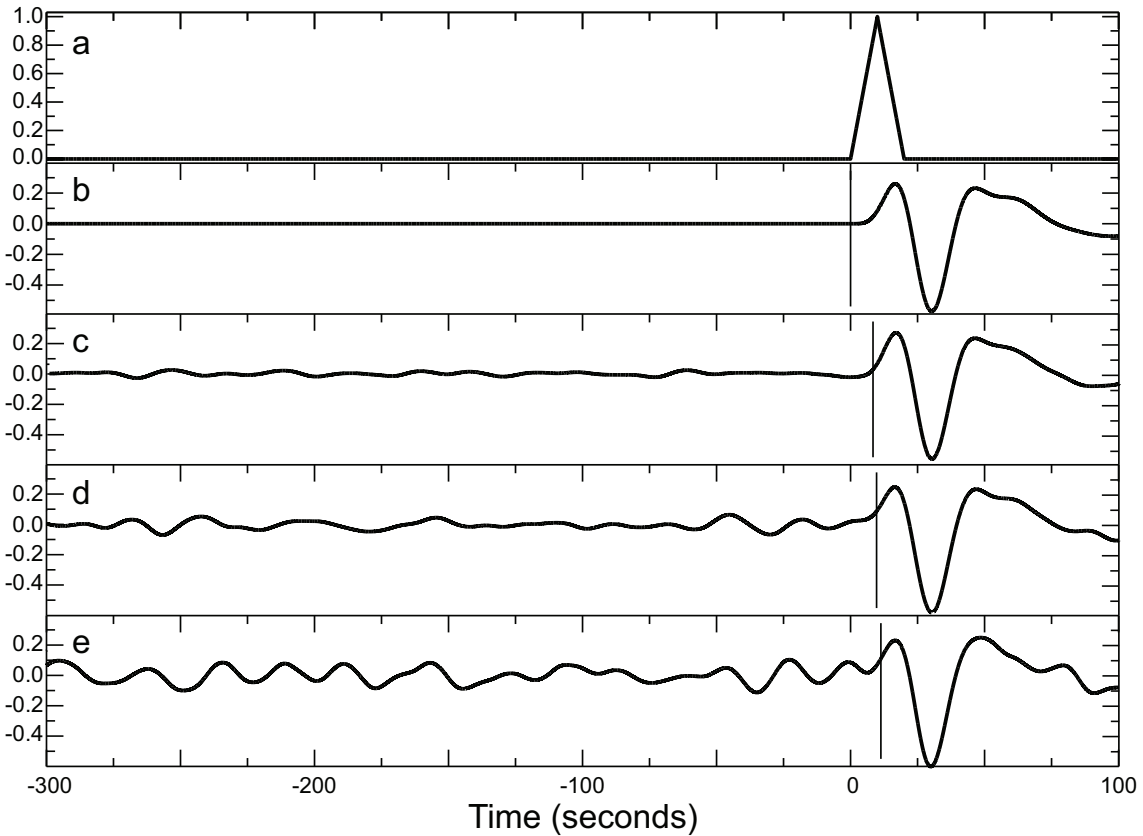
Supplementary Figure S6: Vertical component displacement spectra for four stations (TA.I23K, TA.POKR, AK.NEA2, TA.H24K), showing the enhancement in low-frequency amplitudes for the 2015-09-12 M_w 3.8 (depth 21 km) VLFE (solid black) in comparison with the 2015-10-31 M_w 3.4 (depth 25 km) earthquake (solid red). The signal spectra are calculated for a time window spanning from the origin time to 600 seconds. The noise spectra, plotted as dashed curves, are calculated for a time window of 600 seconds preceding the origin time. The vertical lines mark the limits of the bandpass used for the VLFE moment tensor inversion: 20–50 s. The four stations here are among those used within the moment tensor inversion (Figure S3a). Note that the two events are separated by 91 km (Figure 1a), resulting in different source-station distances, as labeled above each subplot. The depths are estimated from moment tensor inversion as 21 km (VLFE) and 25 km (EQ). The catalog magnitudes, estimated from high-frequency waveforms, are M_1 2.6 (VLFE) and M_1 3.5 (EQ) (Table S1).



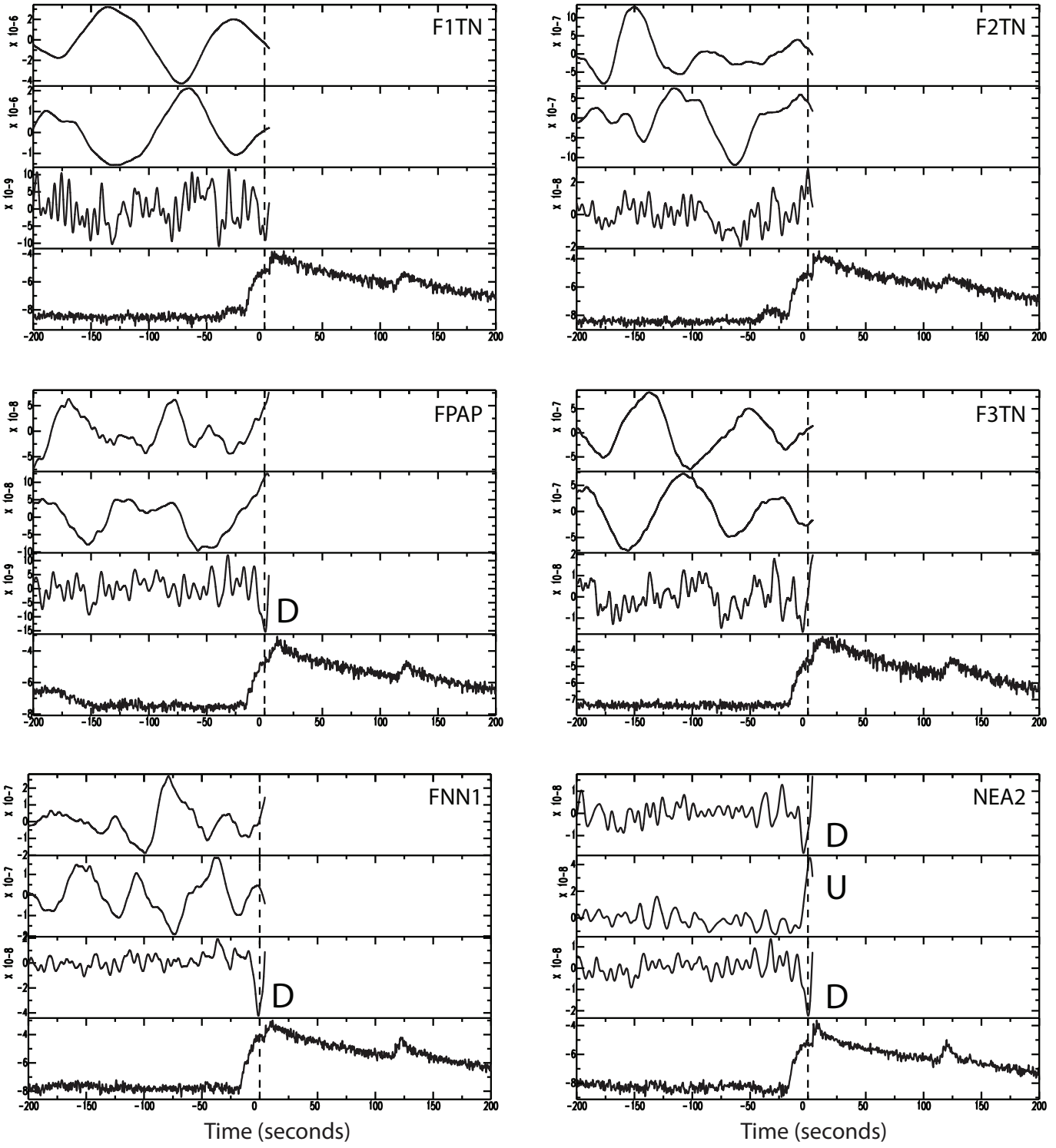
Supplementary Figure S7: Earthquake sequences associated with (a) the M_w 3.7 2016 earthquake and (b) a M_w 5.0 earthquake on 2014-08-31. (a) Network matched filter catalog of earthquakes in the 2016 sequence. (top) Magnitude (M_l) vs. time for the 2016 earthquake sequence. (bottom) Cumulative seismicity over time for the 2016 earthquake sequence. Note that the rate of foreshocks is accelerating up until the time of the mainshock. Most earthquakes do not have foreshock sequences, as seen here. (b) Same as (a), but for the 2014 earthquake.



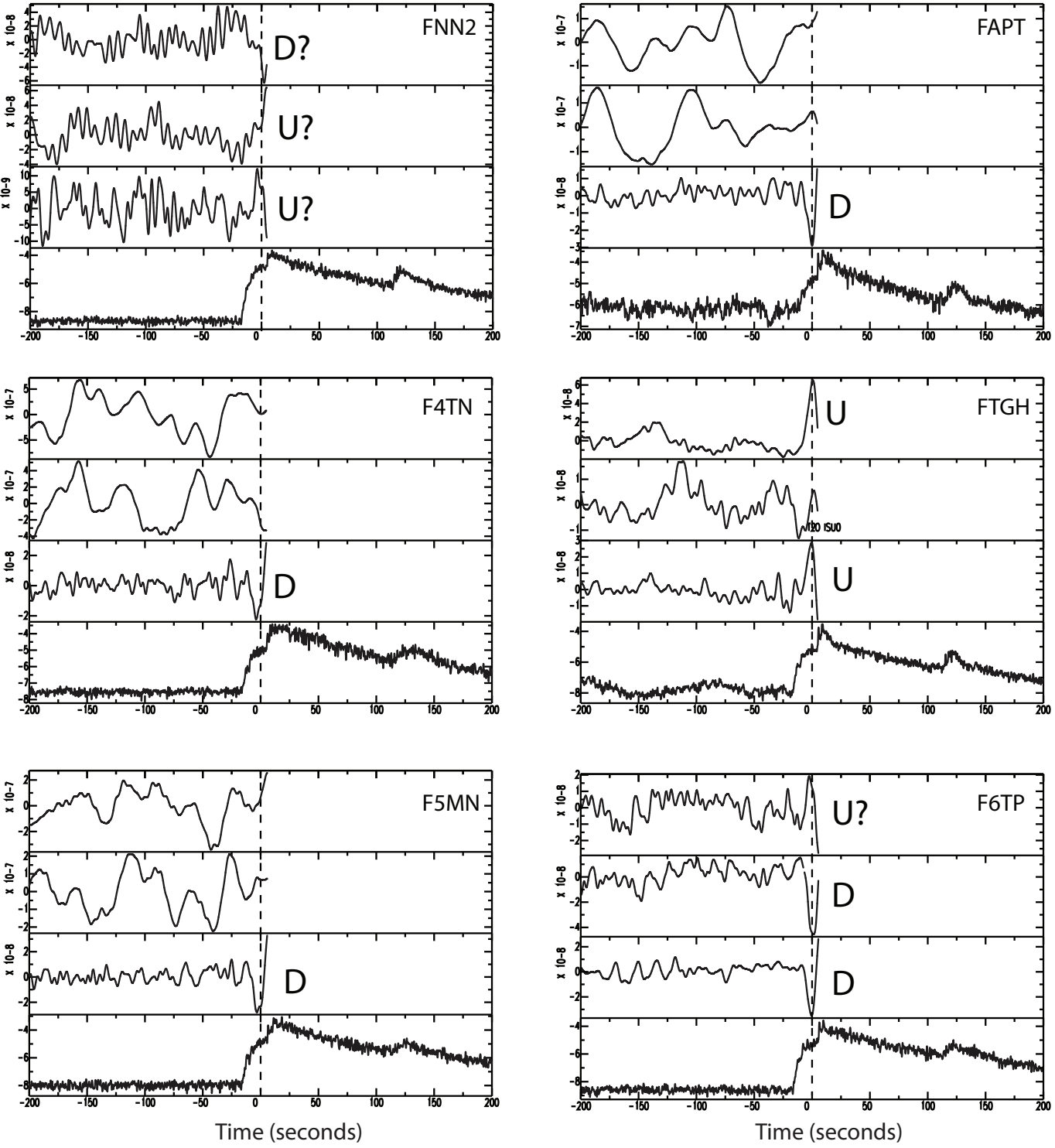
Supplementary Figure S8: Estimated exponent k (Figure S16) for stations <80 km from the epicenter of the 2016 event. Top is for the transverse component; bottom is for the vertical component.



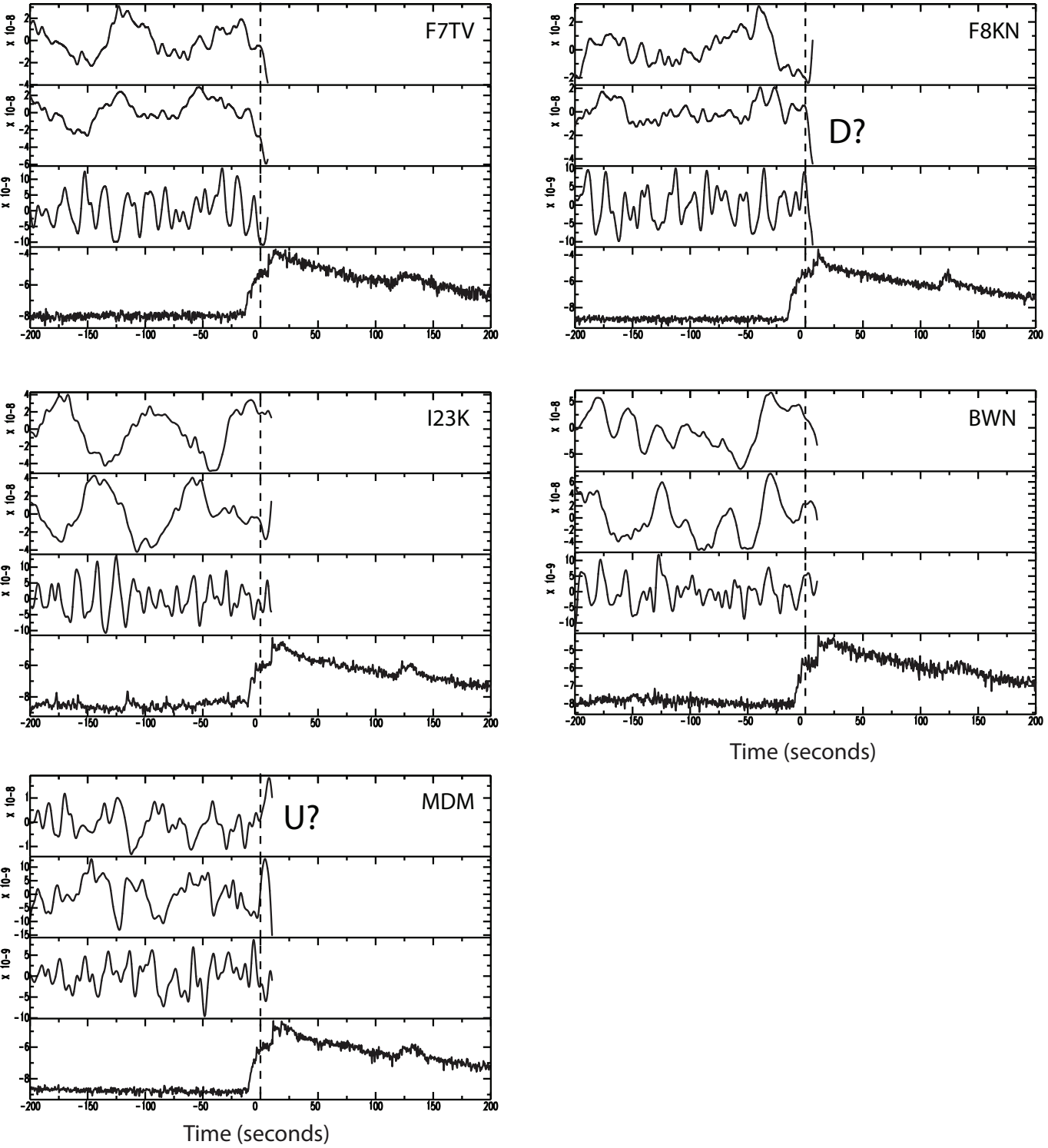
Supplementary Figure S9: A synthetic test illustrating the influence of noise levels on the delay in the LFF onset time pick. (a) An artificial input signal that is a triangle with total width of 20 seconds; the triangle starts at time $t = 0$. (b) Input signal filtered 20–100 s with no noise. The LFF time pick is 0 s. (c) Same as (b) but with $\sim 10\%$ of signal-to-noise (Gaussian noise). The LFF time pick is 8.3 s. (d) Same as (b) but with $\sim 20\%$ noise; the time pick is 9.6 s. (e) Same as (b) but with $\sim 40\%$ noise; the time pick is 11.2 s. These results indicate that the LFF onset time pick will be delayed by 8–12 s from the actual LFF onset. See Tables S4 and S5.



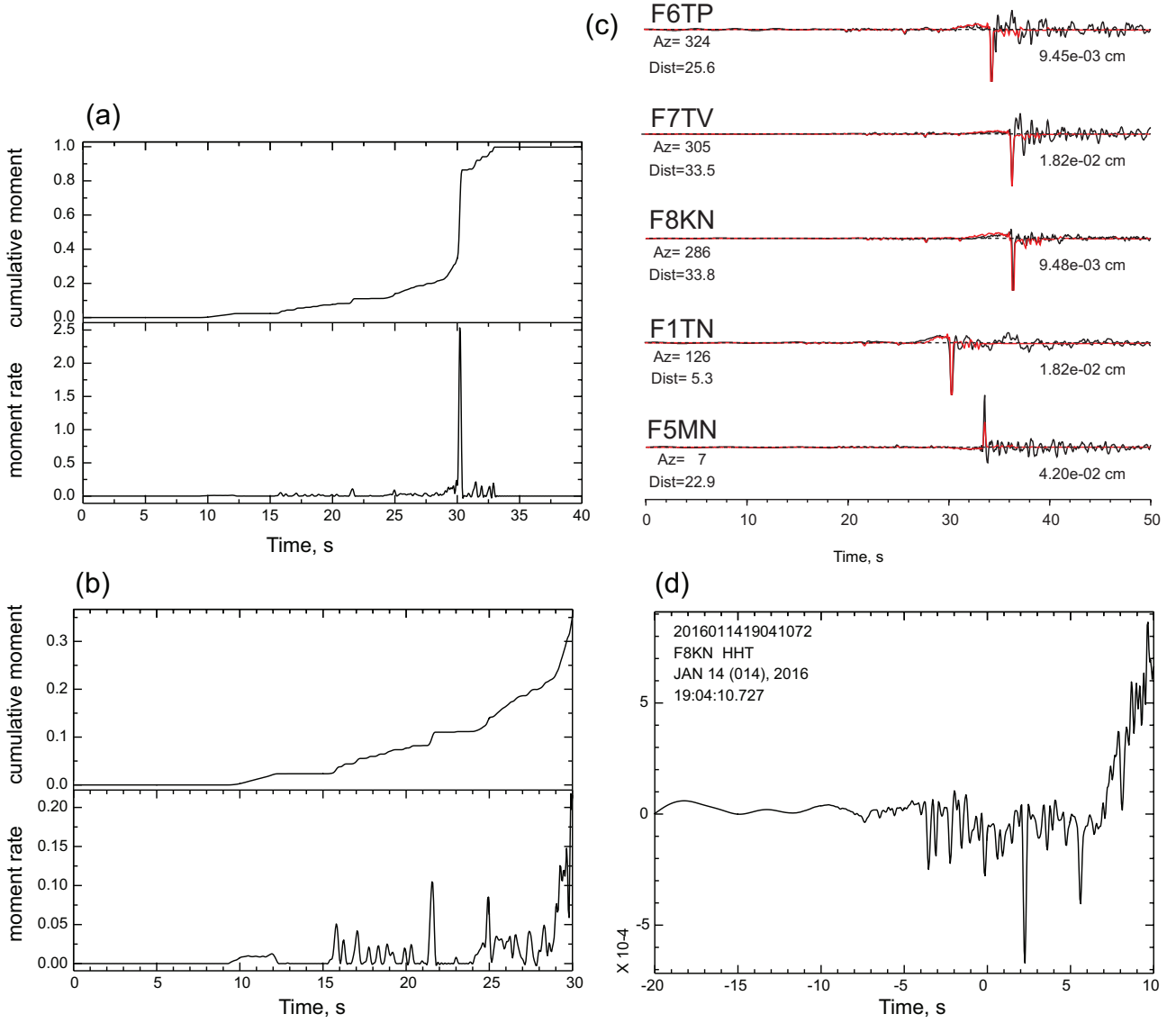
Supplementary Figure S10: Additional examples of waveforms for the 2016 event (Figures S10–S12), similar to Figure 2b. Each subplot has four time series; the dashed line at $t = 0$ is the origin time of the $M_w 3.7$ earthquake. The bottom is the log-scaled envelope of the 2–8 Hz vertical component seismogram; units show the base-10 exponent of m/s (e.g., -4 is 10^{-4} m/s). The top three are the east (top), north (middle), and vertical (bottom) component seismograms (units m/s), causal-filtered 20–100 s and cut at the P arrival time for the earthquake. Our polarity measurement for the low-frequency foreshock (LFF) is labeled. The LFF polarity for the vertical component is listed in Table S3.



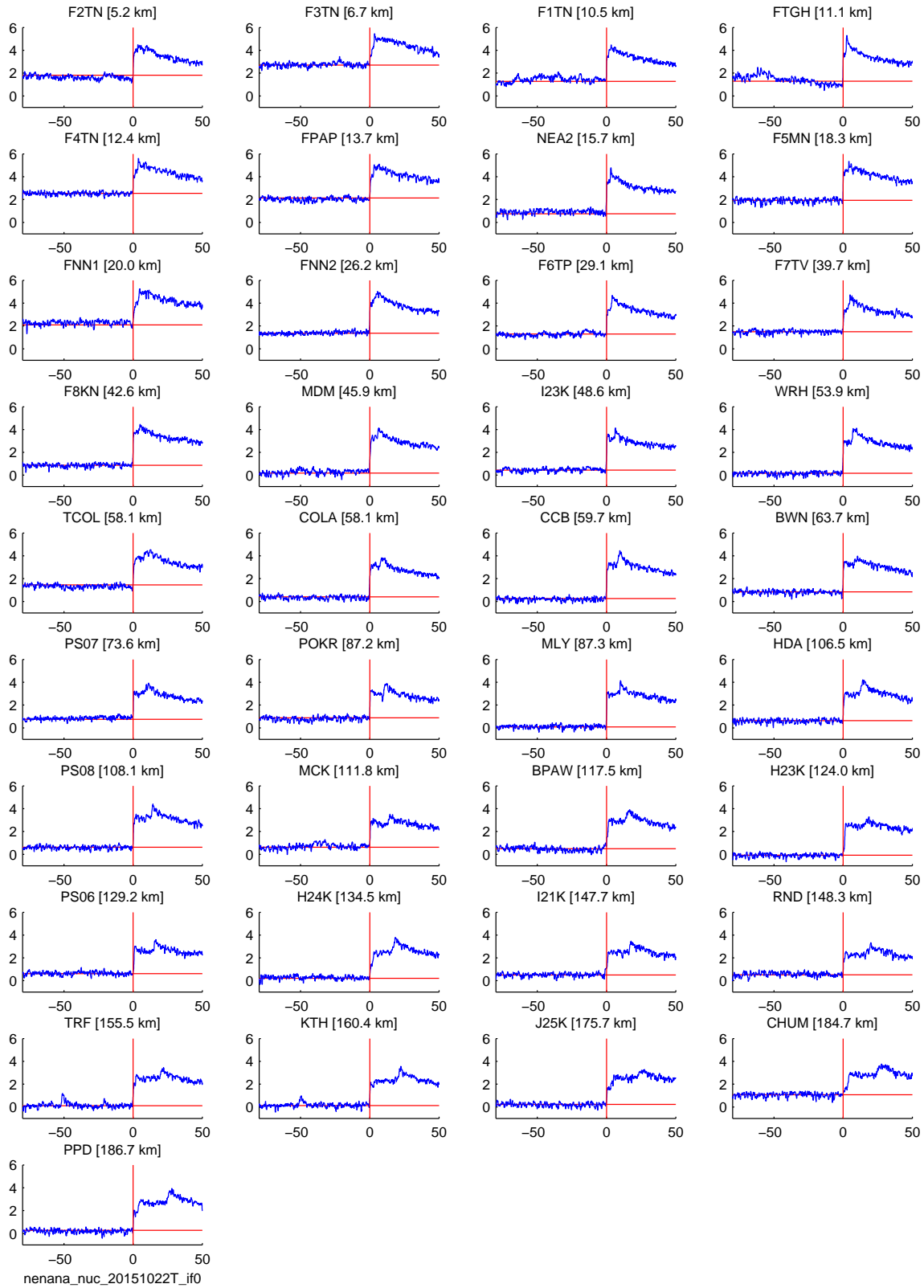
Supplementary Figure S11: Additional examples of waveforms for the 2016 event (Figures S10–S12), similar to Figure 2b. Each subplot has four time series; the dashed line at $t = 0$ is the origin time of the $M_w 3.7$ earthquake. The bottom is the log-scaled envelope of the 2–8 Hz vertical component seismogram; units show the base-10 exponent of m/s (e.g., -4 is 10^{-4} m/s). The top three are the east (top), north (middle), and vertical (bottom) component seismograms (units m/s), causal-filtered 20–100 s and cut at the P arrival time for the earthquake. Our polarity measurement for the low-frequency foreshock (LFF) is labeled. The LFF polarity for the vertical component is listed in Table S3.



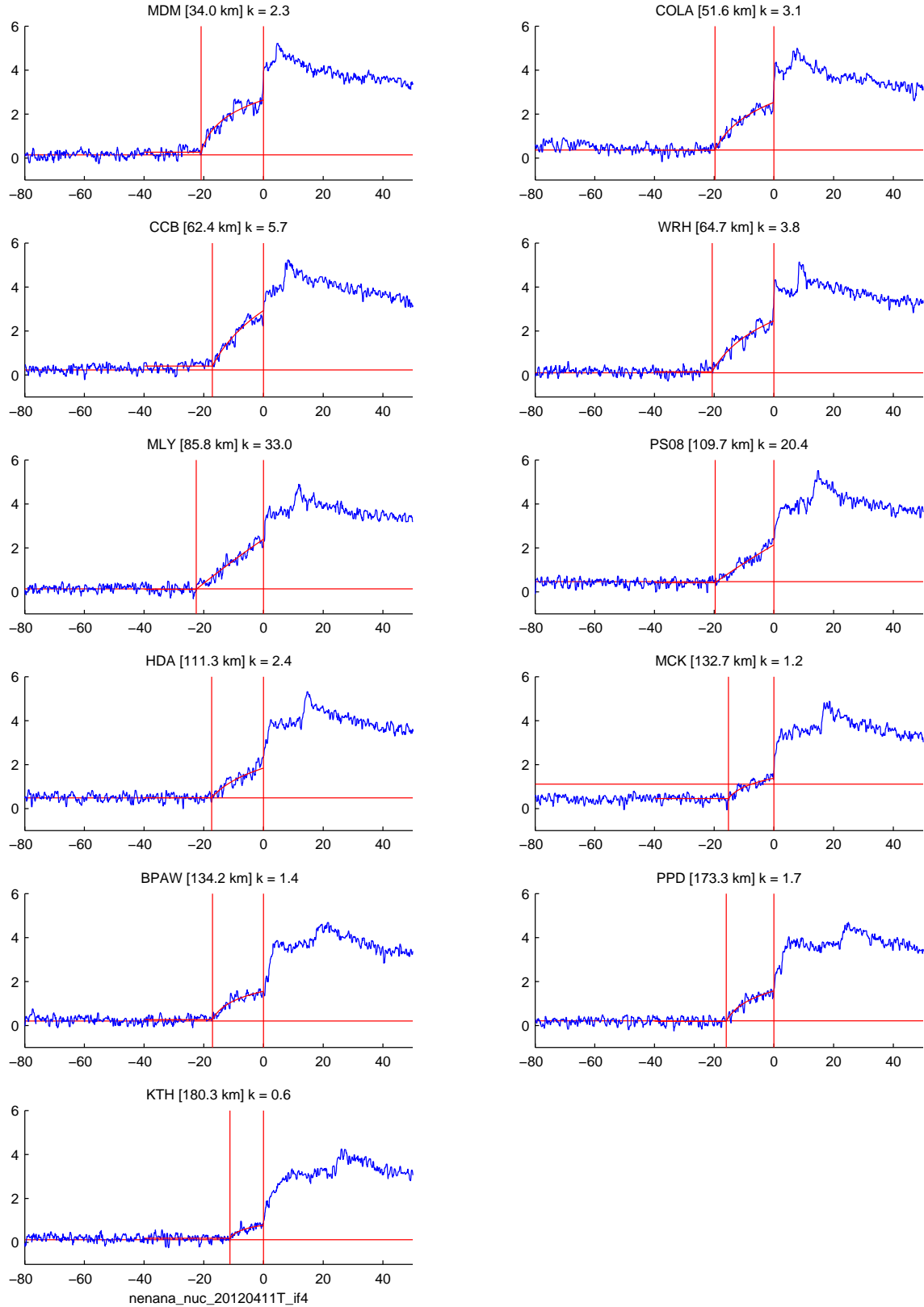
Supplementary Figure S12: Additional examples of waveforms for the 2016 event (Figures S10–S12), similar to Figure 2b. Each subplot has four time series; the dashed line at $t = 0$ is the origin time of the M_w 3.7 earthquake. The bottom is the log-scaled envelope of the 2–8 Hz vertical component seismogram; units show the base-10 exponent of m/s (e.g., -4 is 10^{-4} m/s). The top three are the east (top), north (middle), and vertical (bottom) component seismograms (units m/s), causal-filtered 20–100 s and cut at the P arrival time for the earthquake. Our polarity measurement for the low-frequency foreshock (LFF) is labeled. The LFF polarity for the vertical component is listed in Table S3.



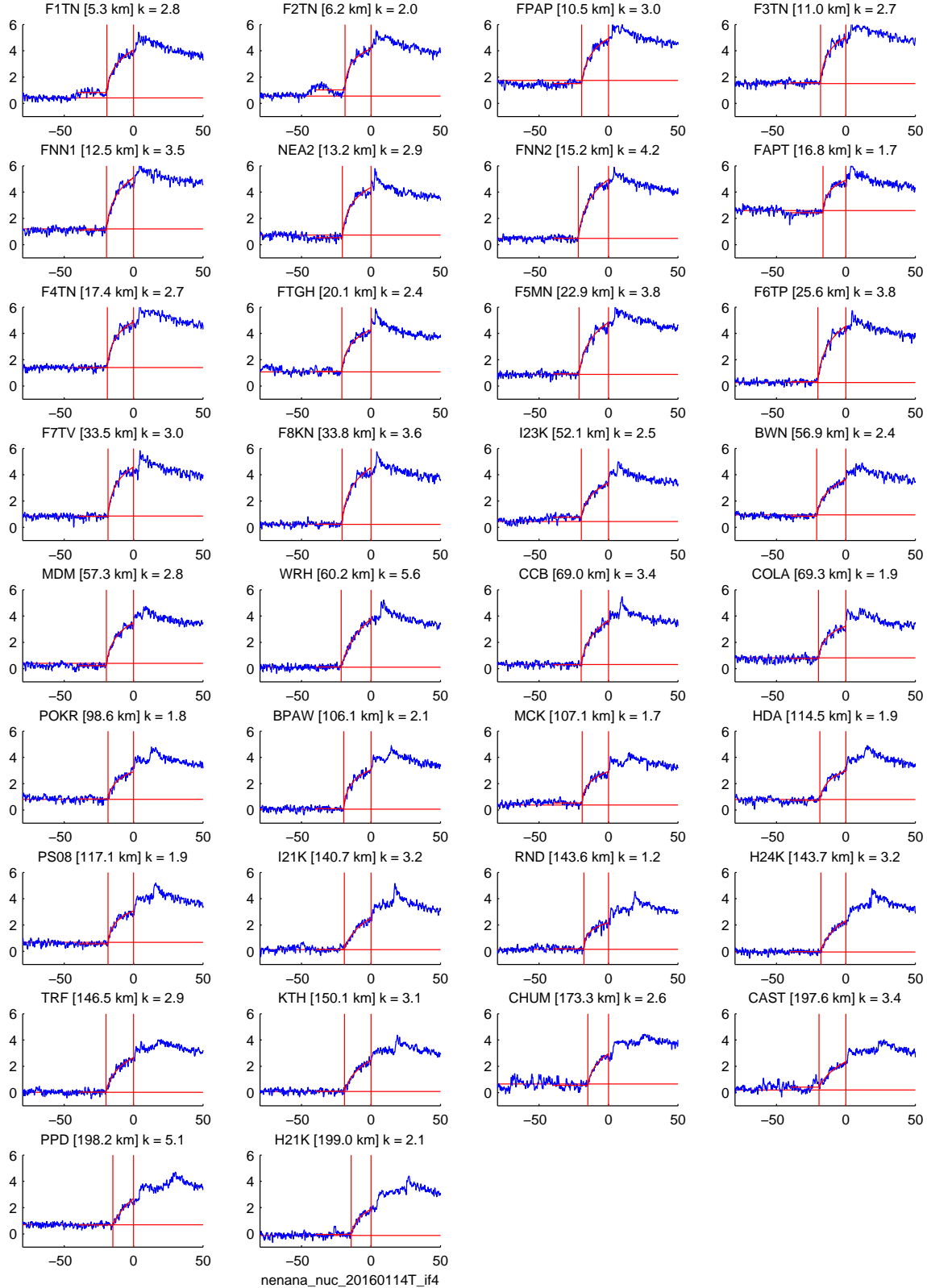
Supplementary Figure S13: Source time function estimation for the 2016 event using high-frequency ($f \leq 4.5$ Hz), transverse-component waveforms at five stations within 35 km of the epicenter: F1TN, F5MN, F6TP, F7TV, F8KN. The data were manually aligned such that the mainshock initiated at $t = 30$ s. Synthetic seismograms were calculated using a standard 1D model for central Alaska (`tactmod`). (a) Cumulative moment function (top) and its derivative, the moment rate function (bottom). (b) Zoom-in of (a) showing the first 30 seconds. (c) Comparison of recorded seismograms (black) and synthetic seismograms (red) calculated using the moment rate function in (a). Text labels show the station azimuth, epicentral distance, and peak amplitude. (d) Transverse displacement seismogram at station F8KN; here $t = 0$ is the mainshock origin time. The high-frequency peaks are correlated with the small peaks in the moment rate function (b). The ramp shape from 7 s to 10 s is partially caused by the near-field term of the mainshock SH wave, which begins with the mainshock P arrival.



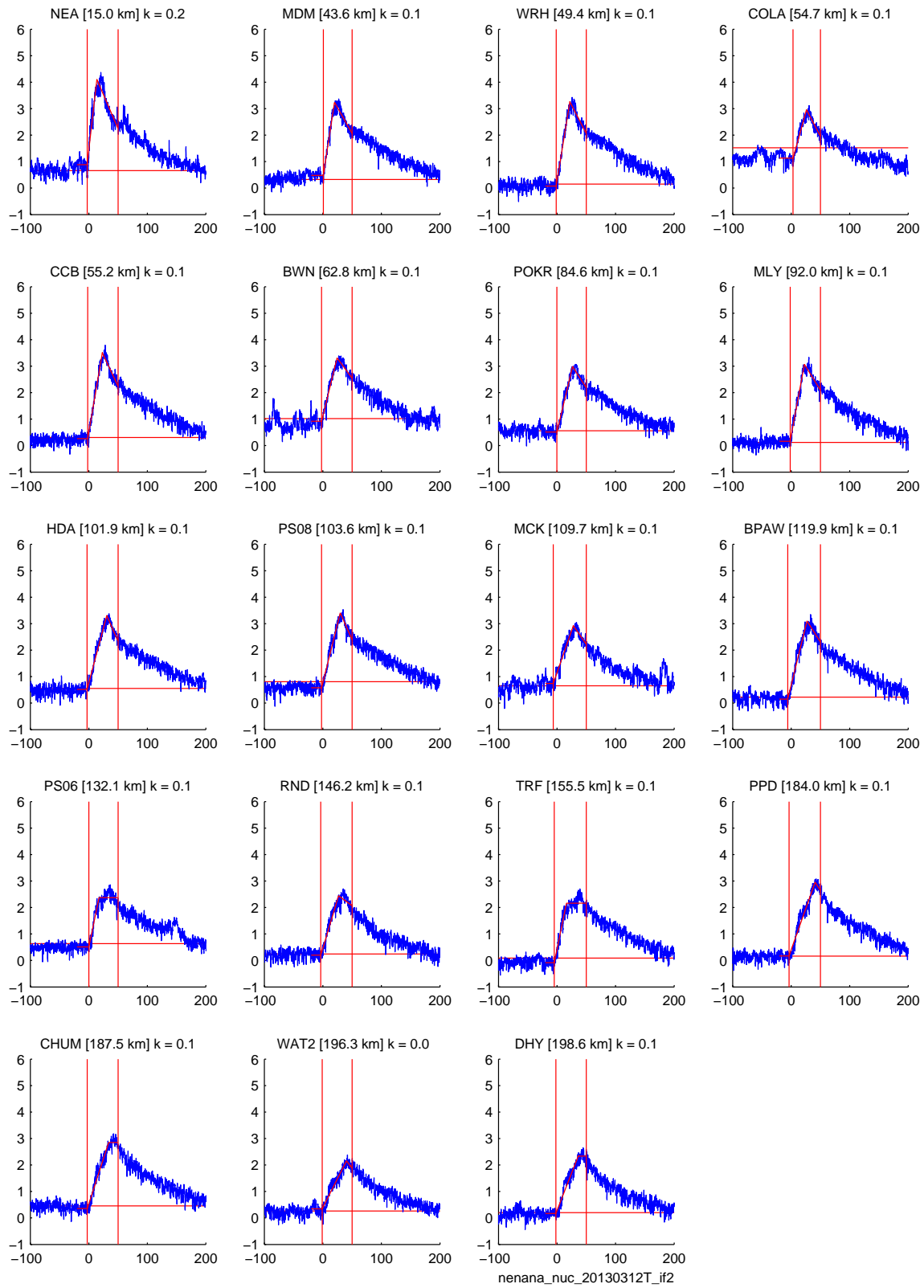
Supplementary Figure S14: Envelopes of high-frequency seismograms for a normal earthquake on 2015-10-22. No coherent signal is visible prior to the P arrival, which is denoted by the vertical red line at $t = 0$. Station MDM is shown in Figure 1b.



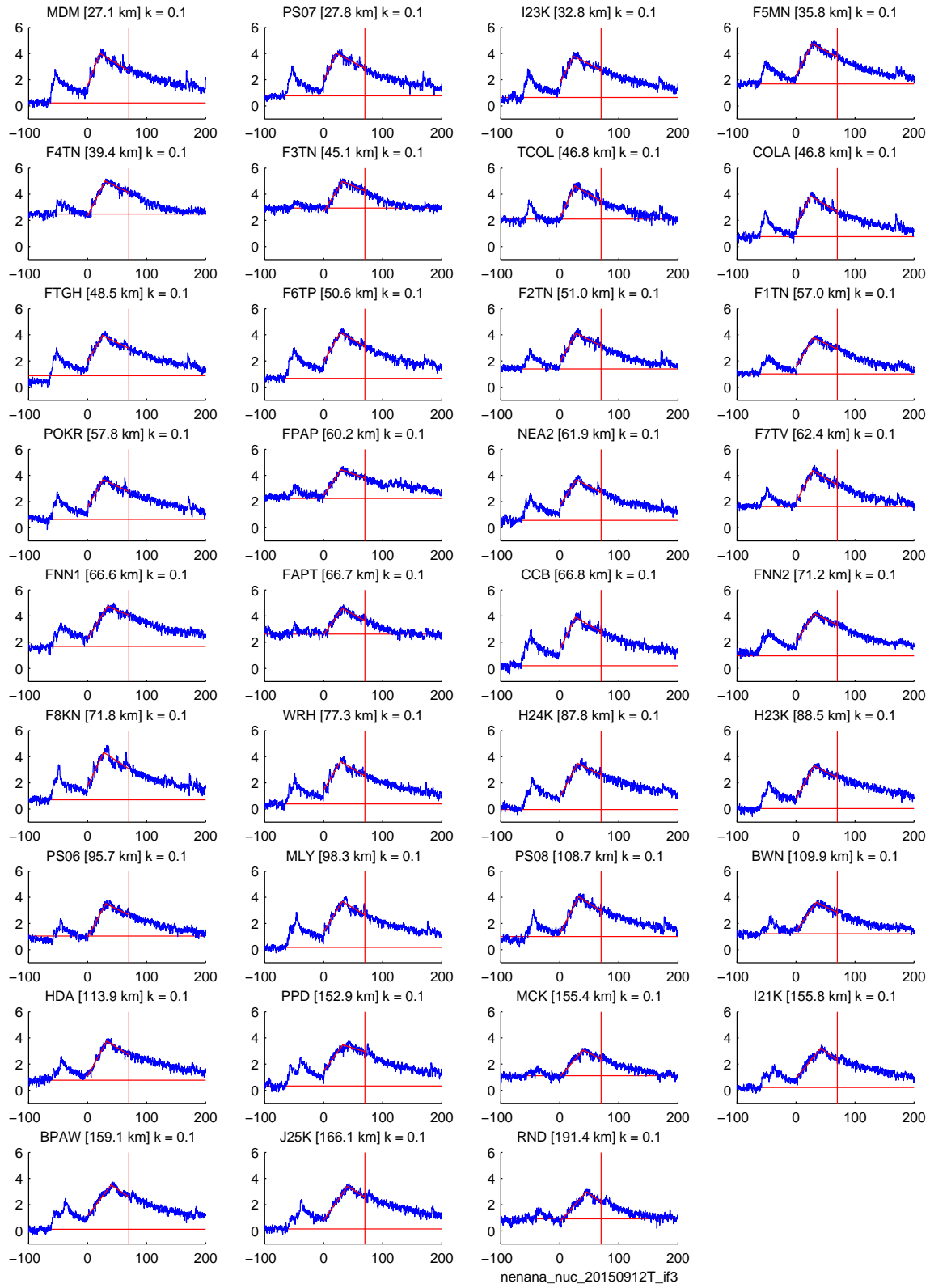
Supplementary Figure S15: Envelopes of high-frequency seismograms for all stations within 200 km of the 2012 event. The vertical red lines span the high-frequency foreshock signals that last approximately 20 s at each station. The estimated value of k , labeled above each subplot, is based on the best-fitting curve of $B(t - t_0)^k$. For comparison with a normal earthquake, see Figure S14. Station MDM is shown in Figure 1b.



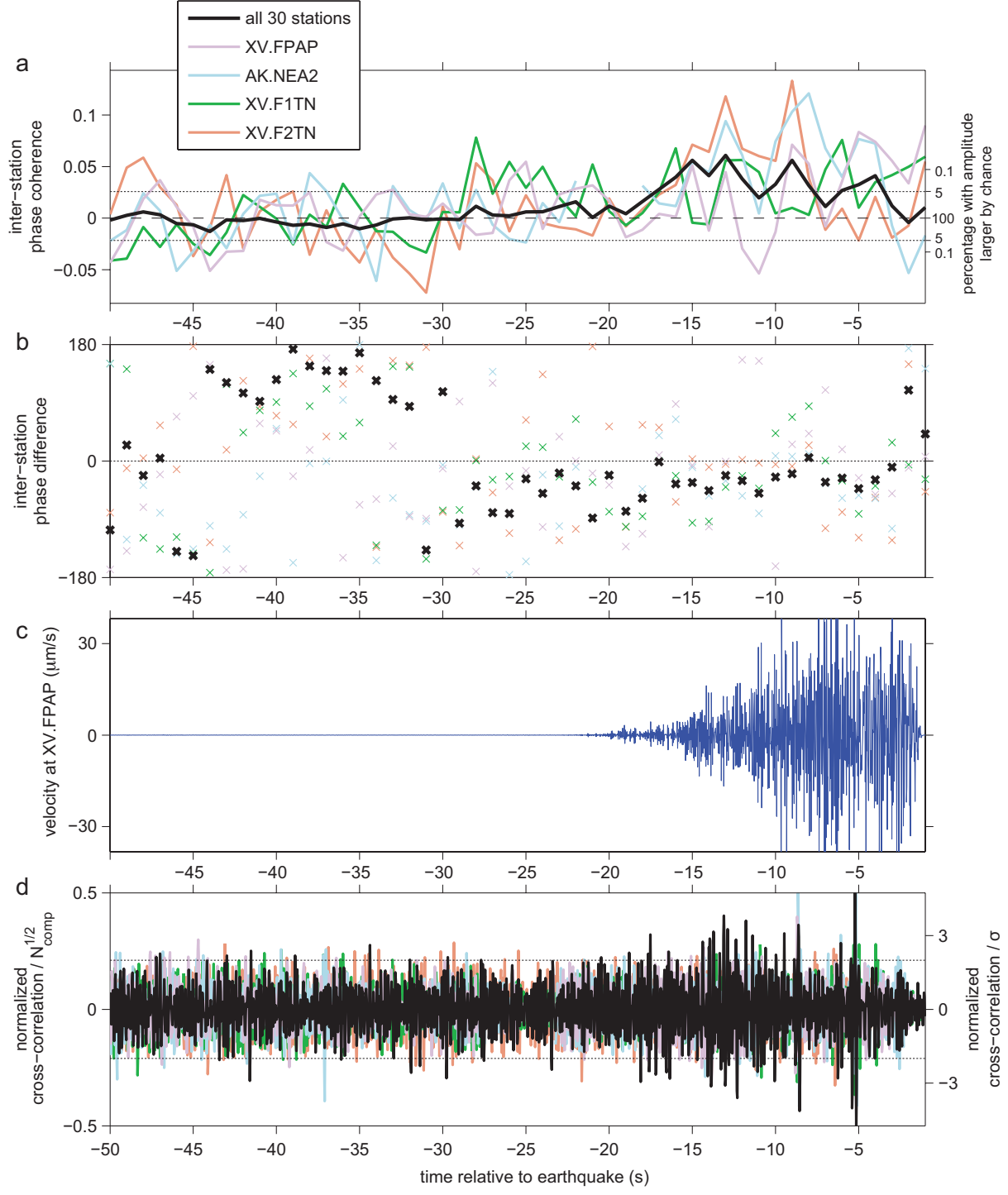
Supplementary Figure S16: Envelopes of high-frequency seismograms for all 34 stations within 200 km of the 2016 event. The vertical red lines span the high-frequency foreshock signals that last approximately 20 s at each station. The estimated value of k , labeled above each subplot, is based on the best-fitting curve of $B(t - t_0)^k$. For comparison with a normal earthquake, see Figure S14. Station MDM is shown in Figure 1b.



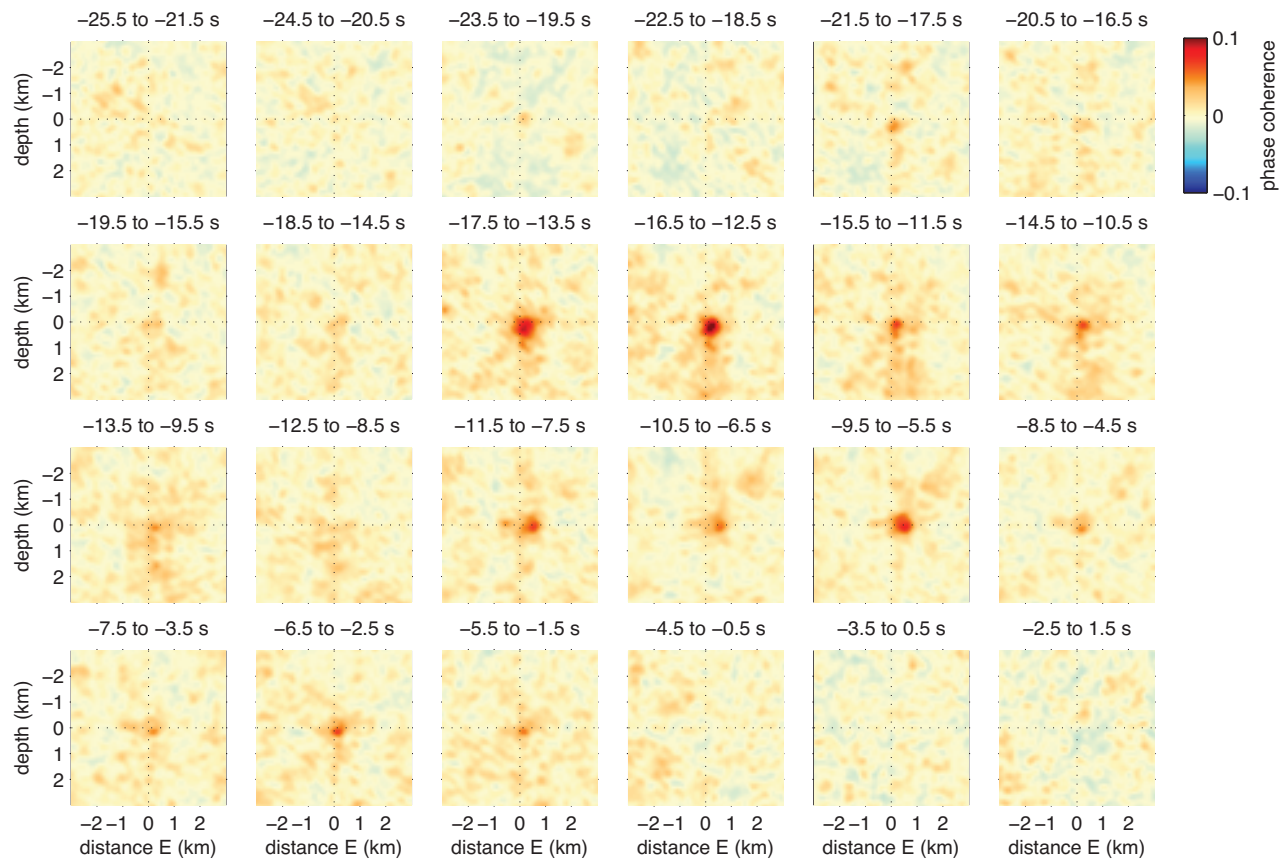
Supplementary Figure S17: Envelopes of high-frequency seismograms for the 2013 VLFE. Compare with the 2015 VLFE in Figure S18. Station MDM is shown in Figure 1b.



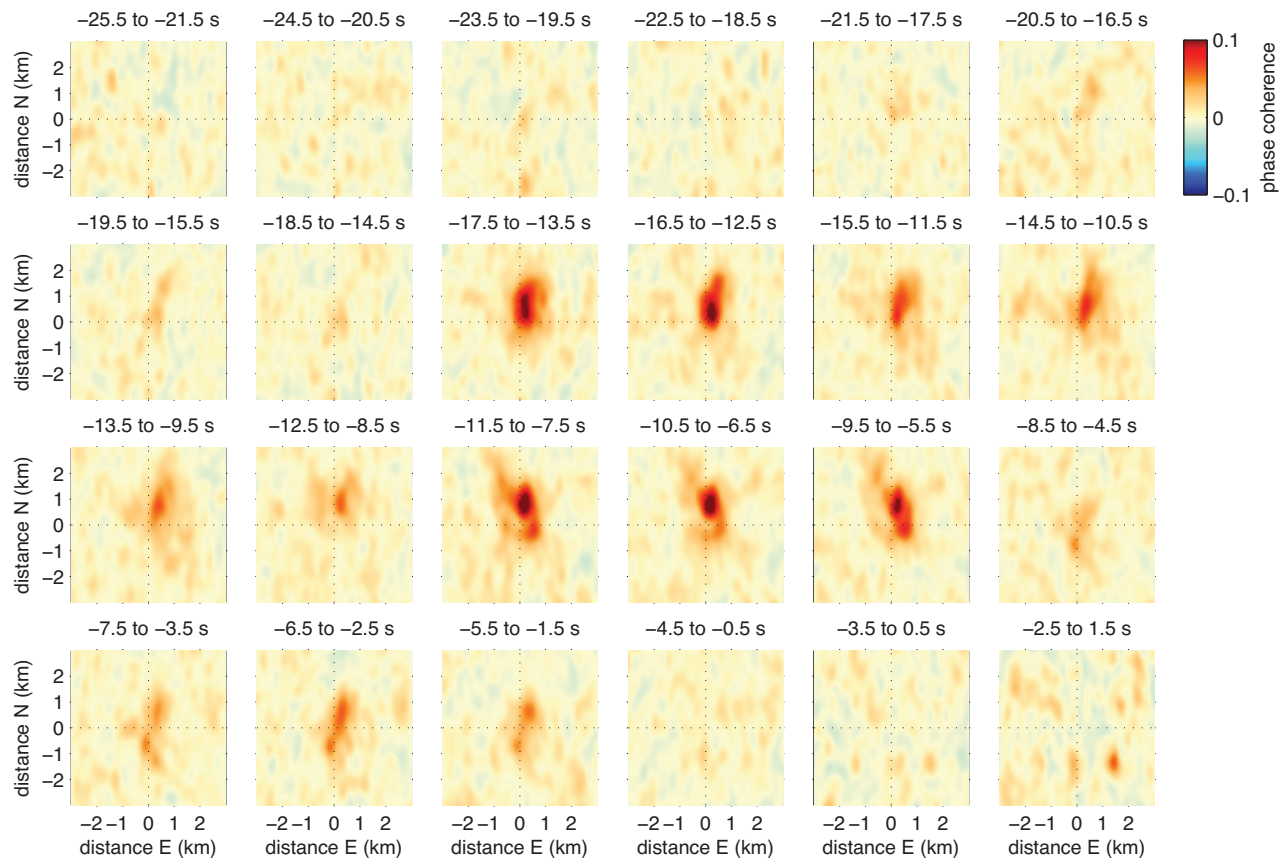
Supplementary Figure S18: Envelopes of high-frequency seismograms for the 2015 VLFE. Station MDM is shown in Figure 1b.



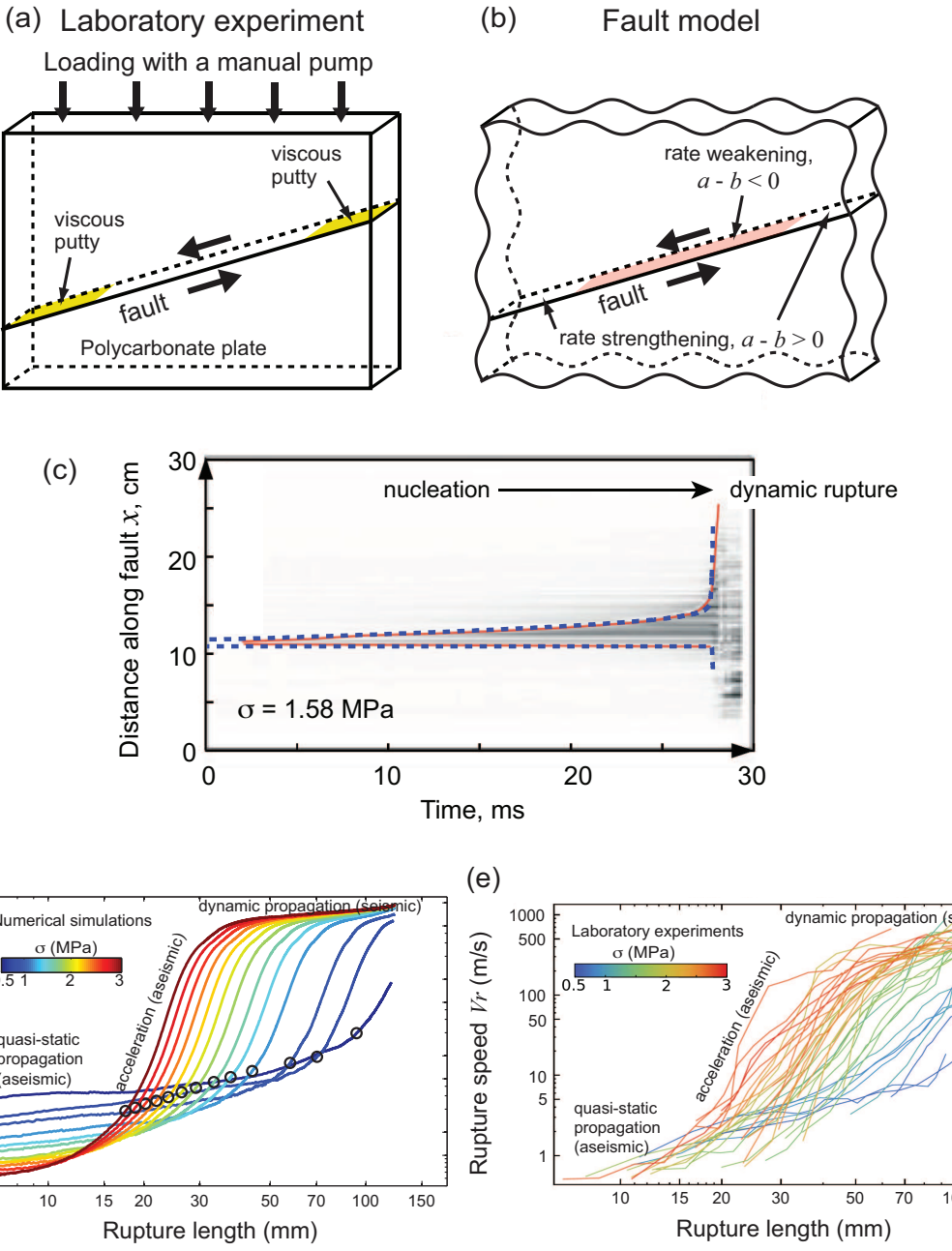
Supplementary Figure S19: Phase coherence between mainshock and high-frequency foreshocks of the 2016 event. (a) 1–10 Hz phase coherence between the mainshock and 4-s windows of the foreshock arrivals. Colored curves for station pairs including the indicated stations. The black curve averages over all available stations. (b) Averaged phase difference between the cross-correlations. (c) Velocity seismogram at XV.FPAP. (d) 1–10 Hz cross-correlation between the mainshock signals and the foreshocks, for individual stations (colors) and averaged over all stations (black).



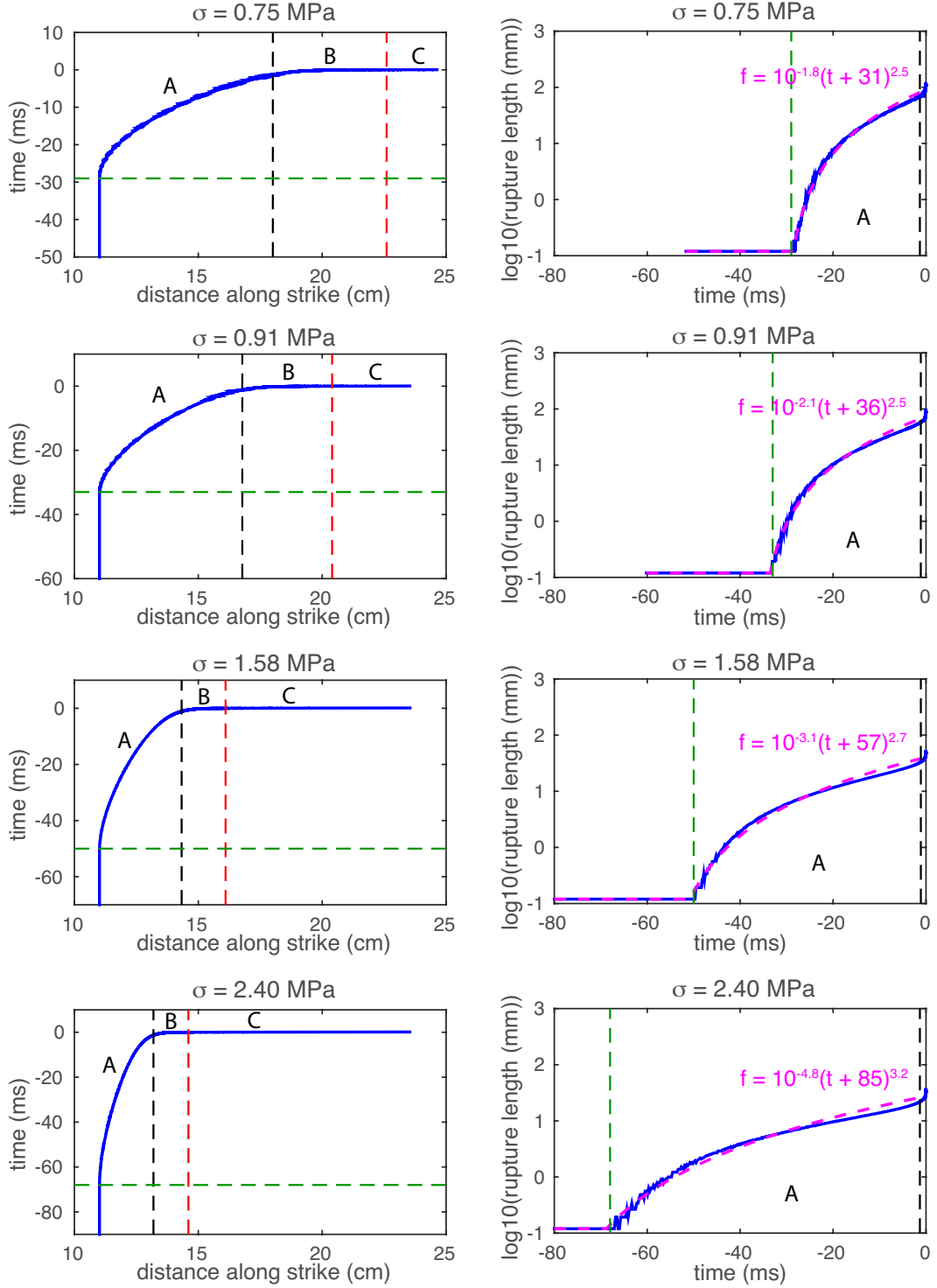
Supplementary Figure S20: Phase coherence between mainshock and high-frequency foreshocks of the 2016 event. Phase coherence is plotted as a function of foreshock location in an east-west oriented vertical plane. This plane has zero north-south offset from the mainshock.



Supplementary Figure S21: Phase coherence between mainshock and high-frequency foreshocks of the 2016 event. Phase coherence is plotted as a function of foreshock location in map view. This plane has zero vertical offset from the mainshock.



Supplementary Figure S22: Schematic diagrams illustrating the set-up of (a) the laboratory experiments of *Latour et al.* (2013) and (b) the numerical model of *Kaneko et al.* (2016). (c) Comparison between simulation results (*Kaneko et al.*, 2016), plotted as the blue dashed line, with laboratory results from *Latour et al.* (2013), plotted as the red line and with grayscale to show the light intensity change indicating the actively slipping zone. The curves show the position of the rupture front during a transition from quasi-static nucleation to dynamic rupture. The rupture fronts are defined as the locations of two peak shear stresses: one within the left rate-strengthening patch and the other within the rate-weakening patch. (d)-(e) Characteristics of nucleation phase under different σ in numerical simulations and for 47 stick-slip events in laboratory experiments. Observed and modeled rupture speeds increase with the rupture length. The rupture length is defined as a distance from the edge of the rate-weakening patch at $x = 11$ cm to the rupture front. The evolution of the rupture front under a range of σ closely matches the laboratory results.



Supplementary Figure S23: Evolution of rupture front position (left column) and rupture length (right column) for four simulations from *Kaneko et al.* (2016) for normal stresses of $\sigma = 0.75 \text{ MPa}$ (top), 0.91 MPa , 1.58 MPa , and 2.40 MPa (bottom). The three stages of rupture are labeled as A (quasi-static), B (acceleration), and C (dynamic propagation). The onsets of the quasi-static, acceleration, and dynamic propagation phases are marked by green, black and red dashed lines, respectively. In this figure, $t = 0$ is defined as the time at the end of the acceleration phase, which is graphically defined from Figure S22d. The magenta dashed curve is a power function fit $(B(t - t_0)^k)$, with the best-fitting power function shown by magenta text.